

Hybrid finite difference/finite element version of the immersed boundary method

Boyce E. Griffith

*Leon H. Charney Division of Cardiology, Department of Medicine, New York
University School of Medicine, 550 First Avenue, New York, New York 10016,
USA*

Xiaoyu Luo

*School of Mathematics and Statistics, University of Glasgow, University Gardens,
Glasgow G12 8QW, UK*

Abstract

The immersed boundary (IB) method is a framework for problems in which an elastic structure is immersed in a viscous incompressible fluid. The IB formulation of such problems describes the elasticity of the structure in Lagrangian form, and describes the momentum, viscosity, and incompressibility of the coupled fluid-structure system in Eulerian form. Interaction between Lagrangian and Eulerian variables is by integral transforms with Dirac delta function kernels. When discretized, the Lagrangian equations are approximated on a curvilinear mesh, and the Eulerian equations are approximated on a Cartesian grid. A regularized version of the delta function is used in approximations to the Lagrangian-Eulerian interaction equations. Standard IB methods typically describe the elasticity of the structure using systems of elastic fibers. We introduce a version of the IB method that uses elasticity models with finite element (FE) discretizations. Unlike most other extensions of the IB method to use FE elasticity, however, our approach retains a Cartesian grid finite difference discretization of the incompressible Navier-Stokes equations. The conventional IB method also typically requires the Lagrangian mesh to be finer than the Eulerian grid. Herein, we introduce an approach to discretizing the interaction equations that enables us to use Lagrangian meshes that are significantly coarser than the background Eulerian grid. Results from computational experiments are included that demonstrate the accuracy and efficiency of our methodology.

Key words: immersed boundary method, fluid-structure interaction, finite element method, finite difference method, incompressible elasticity, incompressible flow

Email addresses: boyce.griffith@nyumc.org (Boyce E. Griffith),
xiaoyu.luo@glasgow.ac.uk (Xiaoyu Luo).

1 Introduction

Since its introduction [1, 2], the immersed boundary (IB) method has been widely used to simulate biological fluid dynamics [3] and other problems in which a structure is immersed in a fluid flow [3–5]. In this paper, we consider the IB method for fluid-structure interaction problems involving an elastic body that is immersed in a viscous incompressible fluid [3]. The IB formulation of such problems uses a Lagrangian description of the immersed structure and an Eulerian description of the momentum, viscosity, and incompressibility of the fluid-structure system. Lagrangian and Eulerian variables are coupled by integral transforms with delta function kernels. When the continuous equations are discretized, the Lagrangian equations are approximated on a curvilinear mesh, the Eulerian equations are approximated on a Cartesian grid, and the Lagrangian-Eulerian interaction equations are approximated by replacing the singular delta function with a regularized delta function. One advantage of the IB formulation is that it enables the use of efficient Cartesian grid solvers, such as those based on fast Fourier transform (FFT) or multigrid methods. Another strength of this approach is that it permits nonconforming discretizations of the fluid and structure. Specifically, the IB method does not require dynamically generated body-fitted meshes, a property that is especially useful for problems involving large structural deformations.

In many applications of the IB method, the elasticity of the immersed structure is described by systems of fibers that resist extension, compression, or bending. Such descriptions can be well-suited for the highly anisotropic materials encountered in biological applications. Fiber models can also be convenient to use in practice because they permit an especially simple definition and discretization. The fiber-based approach to elasticity modeling also presents certain challenges. For instance, it can be difficult to incorporate realistic shear properties or experimentally based constitutive laws into fiber models. Nonetheless, the fiber-based modeling approach typically employed with the IB method has facilitated significant work in biofluid dynamics [6–11], including three-dimensional simulations of cardiac fluid dynamics [12–20].

Over the past decade, several distinct research efforts have sought to use more general material models with the IB method. For instance, work is underway to develop an energy functional-based version of the IB method that uses ideas from finite element (FE) methods [21, 22]. A separate line of research led to the development of the immersed finite element (IFE) method [23–25], which can be viewed as a generalization of the IB method in which FE methods are used for both the fluid and the structure. Like the IB method, the IFE method couples Lagrangian and Eulerian variables by discretized integral transforms with regularized delta function kernels, although different families of smoothed kernel functions are generally used by the two methods. Other work has led

to the development of a fully variational IB method that avoids regularized delta functions altogether [26].

In this paper, we introduce an alternative approach to using FE mechanics models with the IB method that combines a Cartesian grid finite difference method for incompressible fluid dynamics with a nodal FE method for non-linear elasticity. We use the continuous IB formulation introduced by Boffi et al. [26], and we consider two weak formulations of the equations of motion suitable for use with C^0 FE methods for elasticity. One of these formulations, referred to herein as the unified weak form, is similar to those used by earlier IB-like methods [23–26]. The other, which does not appear to have been used previously to construct a numerical scheme, partitions the elastic force density into an *internal force* that is supported throughout the immersed elastic structure, and a *transmission force* that is supported only on the surface of the immersed structure. We provide numerical examples that demonstrate that improvements in accuracy can be obtained by employing the partitioned formulation instead of the unified formulation, especially for Lagrangian meshes that are relatively coarse compared to the Eulerian grid.

Conventionally, regularized delta functions are used by the IB and IFE methods both to *spread* the forces generated by the structure directly from the nodes of the Lagrangian mesh to the Eulerian grid, and also to *interpolate* velocities from the Eulerian grid directly to the nodes of the Lagrangian mesh. A limitation of this approach is that if the physical spacing of the Lagrangian nodes is too large in comparison to the background Eulerian grid, severe leaks will develop at fluid-structure interfaces. An empirical rule that seems to prevent such leaks is to require the Lagrangian mesh to be approximately twice as fine as the Eulerian grid [3]. Because high Eulerian resolution is required to capture the thin boundary layers characteristic of high Reynolds number flows, following this empirical rule can require using very dense Lagrangian meshes that can generate significant numerical stiffness in the discretized equations.

A key contribution of this paper is that it introduces a new approach to discretizing the equations of Lagrangian-Eulerian interaction that overcomes this longstanding limitation of the IB method. Specifically, instead of spreading forces from and interpolating velocities to the nodes of the Lagrangian mesh, herein we spread forces from and interpolate velocities to quadrature points located within the interiors of the Lagrangian finite elements. This approach takes advantage of the additional geometrical information provided by the FE description of the structure, which yields approximations not only to the current positions of the nodes of the Lagrangian mesh, but also to the positions of any material points within the structure. Like the conventional IB method [3], our approach satisfies a power identity that implies that the semi-discretized scheme conserves energy during Lagrangian-Eulerian interaction. An important advantage of our approach is that obtaining a watertight structure simply

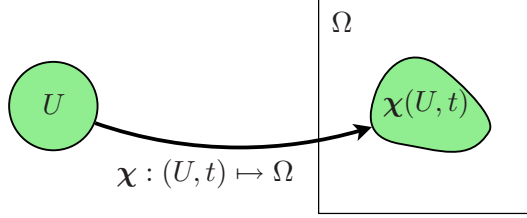


Fig. 1. Lagrangian and Eulerian coordinate systems. The Lagrangian material coordinate domain is U , and the Eulerian physical coordinate domain is Ω . The physical position of material point \mathbf{s} at time t is $\boldsymbol{\chi}(\mathbf{s}, t)$, the physical region occupied by the structure is $\boldsymbol{\chi}(U, t)$, and the physical region occupied by the fluid is $\Omega \setminus \boldsymbol{\chi}(U, t)$.

requires a quadrature scheme with sufficiently many quadrature points to prevent leaks. We present numerical tests that demonstrate that our scheme can yield accurate results even for Lagrangian meshes that are significantly *coarser* than the background Eulerian grid.

2 Continuous formulations

In the IB formulation of problems of fluid-structure interaction, the momentum, velocity, and incompressibility of the coupled fluid-structure system are described in Eulerian form, whereas the elasticity of the immersed structure is described in Lagrangian form. Let $\mathbf{x} = (x_1, x_2, \dots) \in \Omega \subset \mathbb{R}^d$, $d = 2$ or 3 , denote Cartesian physical coordinates, with Ω denoting the physical region that is occupied by the coupled fluid-structure system; let $\mathbf{s} = (s_1, s_2, \dots) \in U \subset \mathbb{R}^d$ denote Lagrangian material coordinates that are attached to the structure, with U denoting the Lagrangian coordinate domain; and let $\boldsymbol{\chi}(\mathbf{s}, t) \in \Omega$ denote the physical position of material point \mathbf{s} at time t . The physical region occupied by the structure at time t is $\boldsymbol{\chi}(U, t) \subseteq \Omega$, and the physical region occupied by the fluid at time t is $\Omega \setminus \boldsymbol{\chi}(U, t)$. See Fig. 1. We do not assume that the Lagrangian coordinates are the initial coordinates of the elastic structure, i.e., that $\boldsymbol{\chi}(\mathbf{s}, 0) = \mathbf{s}$, nor, more generally, do we require that $U \subseteq \Omega$.

To use an Eulerian description of the fluid and a Lagrangian description of the elasticity of the immersed structure, it is necessary to describe the stress of the fluid-structure system in both Eulerian and Lagrangian forms. If $\boldsymbol{\sigma} = \boldsymbol{\sigma}(\mathbf{x}, t)$ is the Cauchy stress tensor of the coupled fluid-structure system, then

$$\boldsymbol{\sigma}(\mathbf{x}, t) = \begin{cases} \boldsymbol{\sigma}^f(\mathbf{x}, t) + \boldsymbol{\sigma}^e(\mathbf{x}, t) & \text{for } \mathbf{x} \in \boldsymbol{\chi}(U, t), \\ \boldsymbol{\sigma}^f(\mathbf{x}, t) & \text{otherwise,} \end{cases} \quad (1)$$

in which $\boldsymbol{\sigma}^f(\mathbf{x}, t)$ is the stress tensor of a viscous incompressible fluid, and $\boldsymbol{\sigma}^e(\mathbf{x}, t)$ is the stress tensor that describes the elasticity of the immersed struc-

ture. The fluid stress tensor is the usual one for a viscous incompressible fluid,

$$\boldsymbol{\sigma}^f = -p\mathbb{I} + \mu \left[\nabla \mathbf{u} + (\nabla \mathbf{u})^T \right], \quad (2)$$

where $p = p(\mathbf{x}, t)$ is the hydrostatic pressure, μ is the dynamic viscosity of the fluid, and $\mathbf{u} = \mathbf{u}(\mathbf{x}, t)$ is the Eulerian fluid velocity field. To describe the elasticity of the structure with respect to the Lagrangian material coordinate system, it is convenient to use the first Piola-Kirchhoff elastic stress tensor $\mathbb{P}^e(\mathbf{s}, t)$, which is defined so that

$$\int_{\partial V} \mathbb{P}^e(\mathbf{s}, t) \mathbf{N} \, dA(\mathbf{s}) = \int_{\partial \boldsymbol{\chi}(V, t)} \boldsymbol{\sigma}^e(\mathbf{x}, t) \mathbf{n} \, da(\mathbf{x}) \quad (3)$$

for any smooth region $V \subset U$, in which $\mathbf{N} = \mathbf{N}(\mathbf{s})$ is the outward unit normal along ∂V , and $\mathbf{n} = \mathbf{n}(\mathbf{x}, t)$ is the outward unit normal along $\partial \boldsymbol{\chi}(V, t)$. For simplicity, we shall restrict our attention to hyperelastic constitutive models, which may be characterized by a strain-energy functional $W^e = W^e(\mathbb{F})$, where $\mathbb{F} = \mathbb{F}(\mathbf{s}, t) = \nabla_{\mathbf{s}} \boldsymbol{\chi}(\mathbf{s}, t) = \frac{\partial \boldsymbol{\chi}}{\partial \mathbf{s}}(\mathbf{s}, t)$ is the deformation gradient associated with the mapping $\boldsymbol{\chi} : (U, t) \mapsto \Omega$. For such constitutive laws, $\mathbb{P}^e(\mathbf{s}, t) = \frac{\partial W^e}{\partial \mathbb{F}}(\mathbf{s}, t)$. See, e.g., Belytschko et al. [27] for further details.

2.1 Strong formulation

The strong form of the equations of motion for the fluid-structure system is:

$$\rho \left(\frac{\partial \mathbf{u}}{\partial t}(\mathbf{x}, t) + \mathbf{u}(\mathbf{x}, t) \cdot \nabla \mathbf{u}(\mathbf{x}, t) \right) = \nabla \cdot \boldsymbol{\sigma}(\mathbf{x}, t) \\ = -\nabla p(\mathbf{x}, t) + \mu \nabla^2 \mathbf{u}(\mathbf{x}, t) + \mathbf{f}^e(\mathbf{x}, t), \quad (4)$$

$$\nabla \cdot \mathbf{u}(\mathbf{x}, t) = 0, \quad (5)$$

$$\mathbf{f}^e(\mathbf{x}, t) = \int_U \nabla_{\mathbf{s}} \cdot \mathbb{P}^e(\mathbf{s}, t) \delta(\mathbf{x} - \boldsymbol{\chi}(\mathbf{s}, t)) \, d\mathbf{s} \\ - \int_{\partial U} \mathbb{P}^e(\mathbf{s}, t) \mathbf{N}(\mathbf{s}) \delta(\mathbf{x} - \boldsymbol{\chi}(\mathbf{s}, t)) \, dA(\mathbf{s}), \quad (6)$$

$$\frac{\partial \boldsymbol{\chi}}{\partial t}(\mathbf{s}, t) = \int_{\Omega} \mathbf{u}(\mathbf{x}, t) \delta(\mathbf{x} - \boldsymbol{\chi}(\mathbf{s}, t)) \, d\mathbf{x}, \quad (7)$$

where ρ is the mass density of the coupled fluid-structure system, $\mathbf{f}^e(\mathbf{x}, t)$ is the Eulerian elastic force density, and $\delta(\mathbf{x}) = \prod_{i=1}^d \delta(x_i)$ is the d -dimensional delta function. We omit the derivation of this formulation of the equations of motion, which was introduced by Boffi et al. [26].

In the equations of motion, Eqs. (4) and (5) are the standard Eulerian incompressible Navier-Stokes equations, except that the right-hand side of the momentum equation, Eq. (4), is augmented by an Eulerian elastic force density, $\mathbf{f}^e(\mathbf{x}, t) = \nabla \cdot \boldsymbol{\sigma}^e(\mathbf{x}, t)$, that is determined from the Lagrangian configuration

of the immersed structure via Eq. (6). The conversion from the Lagrangian to the Eulerian description of the forces generated by the elasticity of the immersed structure is mediated by two integral transforms with delta function kernels. These integral transforms appear in Eq. (6) and convert $\nabla_{\mathbf{s}} \cdot \mathbb{P}^e$, the Lagrangian *internal force density*, and $-\mathbb{P}^e \mathbf{N}$, the Lagrangian *transmission force density*, into equivalent Eulerian densities. Notice that these two Lagrangian force densities have totally different characters: The internal force density is supported throughout U and has units of force per unit volume, whereas the transmission force density is supported only along ∂U and has units of force per unit area. Assuming that $\mathbb{P}^e(\mathbf{s}, t)$ is sufficiently smooth, the internal force acts as a regular (i.e., nonsingular) body force on the fluid and may be treated with higher-order accuracy by the IB method [26, 28]. The transmission force acts as a singular force layer on the fluid, and although this force will induce jumps in the pressure and the derivatives of the velocity along $\partial\chi(U, t)$, such force layers may also be readily treated by the IB method. In many presentations of the IB method for fluid-structure interaction (see, e.g., Peskin [3]), the transmission force is not included in the equations of motion, although its effect must be included, either implicitly or explicitly, in the numerical scheme. The explicit inclusion of the transmission force is the key difference between this formulation and the conventional IB formulation, and facilitates the development of weak forms of the equations.

An integral transform is also used in Eq. (7) to determine the velocity of the immersed elastic structure from the material velocity field $\mathbf{u}(\mathbf{x}, t)$. The defining property of $\delta(\mathbf{x})$ implies that Eq. (7) is equivalent to $\frac{\partial \chi}{\partial t}(\mathbf{s}, t) = \mathbf{u}(\chi(\mathbf{s}, t), t)$, which may be interpreted as the no-slip and no-penetration conditions of a viscous incompressible fluid. Notice, however, that the no-slip and no-penetration conditions do not appear as constraints on the fluid motion. Instead, these conditions determine the motion of the immersed structure.

2.2 Weak formulations

To obtain versions of the equations of motion that allow us to use standard C^0 FE methods for nonlinear elasticity, we consider two different formulations that each employ a weak form of the Lagrangian equations. These two formulations are equivalent in the continuous setting; however, when discretized, they yield numerical schemes that are generally different. Because we use a finite difference scheme to approximate the incompressible Navier-Stokes equations, we do not employ a weak formulation for the Eulerian equations.

We refer to our first weak form of the problem as the *unified weak formulation* because it includes only a single, unified body forcing term that accounts for both the regular internal elastic force density and the singular transmission

elastic force density of the strong form of the equations. This formulation is:

$$\rho \left(\frac{\partial \mathbf{u}}{\partial t} + \mathbf{u} \cdot \nabla \mathbf{u} \right) = -\nabla p + \mu \nabla^2 \mathbf{u} + \mathbf{f}, \quad (8)$$

$$\nabla \cdot \mathbf{u} = 0, \quad (9)$$

$$\mathbf{f}(\mathbf{x}, t) = \int_U \mathbf{F}(\mathbf{s}, t) \delta(\mathbf{x} - \boldsymbol{\chi}(\mathbf{s}, t)) \, \mathrm{d}\mathbf{s}, \quad (10)$$

$$\int_U \mathbf{F}(\mathbf{s}, t) \cdot \mathbf{V}(\mathbf{s}) \, \mathrm{d}\mathbf{s} = - \int_U \mathbb{P}^e(\mathbf{s}, t) : \nabla_{\mathbf{s}} \mathbf{V}(\mathbf{s}) \, \mathrm{d}\mathbf{s}, \quad \forall \mathbf{V}(\mathbf{s}), \quad (11)$$

$$\frac{\partial \boldsymbol{\chi}}{\partial t}(\mathbf{s}, t) = \int_{\Omega} \mathbf{u}(\mathbf{x}, t) \delta(\mathbf{x} - \boldsymbol{\chi}(\mathbf{s}, t)) \, \mathrm{d}\mathbf{x}, \quad (12)$$

where $\mathbf{f}(\mathbf{x}, t)$ and $\mathbf{F}(\mathbf{s}, t)$ are the Eulerian and Lagrangian total elastic force densities, and $\mathbf{V}(\mathbf{s})$ is an arbitrary Lagrangian test function that is not assumed to vanish on ∂U . This weak form of the equations of motion is similar to the formulation employed in the IFE method [23–25] and the fully variational IB method [26]. Notice that $\mathbf{F}(\mathbf{s}, t)$ includes the effects of both the internal and transmission force densities of the strong form of the equations in the sense that

$$\int_U \mathbf{F}(\mathbf{s}, t) \cdot \mathbf{V}(\mathbf{s}) \, \mathrm{d}\mathbf{s} = - \int_U \mathbb{P}^e(\mathbf{s}, t) : \nabla_{\mathbf{s}} \mathbf{V}(\mathbf{s}) \, \mathrm{d}\mathbf{s} \quad (13)$$

$$= \int_U (\nabla \cdot \mathbb{P}^e(\mathbf{s}, t)) \cdot \mathbf{V}(\mathbf{s}) \, \mathrm{d}\mathbf{s} - \int_{\partial U} (\mathbb{P}^e(\mathbf{s}, t) \mathbf{N}(\mathbf{s})) \cdot \mathbf{V}(\mathbf{s}) \, \mathrm{d}A(\mathbf{s}), \quad (14)$$

for any $\mathbf{V}(\mathbf{s})$.

Our second weak form of the problem, which we refer to as the *partitioned weak formulation*, is similar to the unified formulation, except that it treats the internal and transmission elastic force densities separately, as follows:

$$\rho \left(\frac{\partial \mathbf{u}}{\partial t} + \mathbf{u} \cdot \nabla \mathbf{u} \right) = -\nabla p + \mu \nabla^2 \mathbf{u} + \mathbf{g} + \mathbf{t}, \quad (15)$$

$$\nabla \cdot \mathbf{u} = 0, \quad (16)$$

$$\mathbf{g}(\mathbf{x}, t) = \int_U \mathbf{G}(\mathbf{s}, t) \delta(\mathbf{x} - \boldsymbol{\chi}(\mathbf{s}, t)) \, \mathrm{d}\mathbf{s}, \quad (17)$$

$$\begin{aligned} \int_U \mathbf{G}(\mathbf{s}, t) \cdot \mathbf{V}(\mathbf{s}) \, \mathrm{d}\mathbf{s} &= - \int_U \mathbb{P}^e(\mathbf{s}, t) : \nabla_{\mathbf{s}} \mathbf{V}(\mathbf{s}) \, \mathrm{d}\mathbf{s} \\ &\quad + \int_{\partial U} \mathbb{P}^e(\mathbf{s}, t) \mathbf{N}(\mathbf{s}) \cdot \mathbf{V}(\mathbf{s}) \, \mathrm{d}A(\mathbf{s}), \quad \forall \mathbf{V}(\mathbf{s}), \end{aligned} \quad (18)$$

$$\mathbf{t}(\mathbf{x}, t) = \int_{\partial U} \mathbf{T}(\mathbf{s}, t) \delta(\mathbf{x} - \boldsymbol{\chi}(\mathbf{s}, t)) \, \mathrm{d}A(\mathbf{s}), \quad (19)$$

$$\mathbf{T} = -\mathbb{P}^e \mathbf{N}, \quad (20)$$

$$\frac{\partial \boldsymbol{\chi}}{\partial t}(\mathbf{s}, t) = \int_{\Omega} \mathbf{u}(\mathbf{x}, t) \delta(\mathbf{x} - \boldsymbol{\chi}(\mathbf{s}, t)) \, \mathrm{d}\mathbf{x}, \quad (21)$$

where $\mathbf{g}(\mathbf{x}, t)$ and $\mathbf{G}(\mathbf{s}, t)$ are the Eulerian and Lagrangian internal elastic force densities, $\mathbf{t}(\mathbf{x}, t)$ and $\mathbf{T}(\mathbf{s}, t)$ are the Eulerian and Lagrangian transmis-

sion elastic force densities, and $\mathbf{V}(\mathbf{s})$ is an arbitrary Lagrangian test function. Notice that here, $\mathbf{T}(\mathbf{s}, t)$ is equal to the transmission force density of the strong formulation, and that $\mathbf{G}(\mathbf{s}, t)$ is weakly equivalent to the internal force density of the strong form of the equations, as can be shown by integrating the right-hand-side of Eq. 18 by parts.

3 Spatial discretization

We consider only the two-dimensional case for the remainder of the paper. The extension to the case $d = 3$ is straightforward, and implementations for $d = 2$ and 3 are provided by the open-source IBAMR software [29].

3.1 Eulerian discretization

To discretize the incompressible Navier-Stokes equations in space, we employ a two-dimensional staggered-grid finite difference scheme, which yields superior accuracy when used with the IB method as compared to collocated discretizations (i.e., purely cell- or node-centered schemes) [30]. To simplify the exposition, we assume that Ω is the unit square and is discretized on a regular $N \times N$ Cartesian grid with grid spacings $\Delta x_1 = \Delta x_2 = h = \frac{1}{N}$. Let (i, j) label the individual Cartesian grid cells for integer values of i and j , $0 \leq i, j < N$. The components of the Eulerian velocity field $\mathbf{u} = (u_1, u_2)$ are approximated at the centers of the x_1 - and x_2 -edges of the Cartesian grid cells, i.e., at positions $\mathbf{x}_{i-\frac{1}{2},j} = (ih, (j + \frac{1}{2})h)$ and $\mathbf{x}_{i,j-\frac{1}{2}} = ((i + \frac{1}{2})h, jh)$, respectively. A staggered scheme is also used for the Eulerian body force $\mathbf{f} = (f_1, f_2)$. We use the notation $(u_1)_{i-\frac{1}{2},j}$, $(u_2)_{i,j-\frac{1}{2}}$, $(f_1)_{i-\frac{1}{2},j}$, and $(f_2)_{i,j-\frac{1}{2}}$ to denote the discrete values of \mathbf{u} and \mathbf{f} . The pressure p is approximated at the centers of the Cartesian grid cells.

Let $\nabla_h \cdot \mathbf{u} \approx \nabla \cdot \mathbf{u}$, $\nabla_h p \approx \nabla p$, and $\nabla_h^2 \mathbf{u} \approx \nabla^2 \mathbf{u}$ respectively denote standard second-order accurate finite difference approximations to the divergence, gradient, and Laplace operators [31]. In this approach, $\nabla_h \cdot \mathbf{u}$ is defined at cell centers, whereas both $\nabla_h p$ and $\nabla_h^2 \mathbf{u}$ are defined at cell edges. We use a staggered-grid version [30, 31] of the xsPPM7 variant [32] of the piecewise parabolic method (PPM) [33] to discretize the nonlinear advection terms. Where needed, physical boundary conditions are implemented as described by Griffith [31].

If \mathbf{u} and \mathbf{v} are discrete staggered-grid vector fields, we denote by $[\mathbf{u}]$ and $[\mathbf{v}]$ the corresponding vectors of grid values. If Ω has periodic boundaries, we define

the discrete L^2 inner product on Ω by

$$(\mathbf{u}, \mathbf{v})_{\mathbf{x}} = [\mathbf{u}]^T [\mathbf{v}] h^2. \quad (22)$$

Minor adjustments to this definition are required when nonperiodic physical boundary conditions are used [31].

3.2 Lagrangian discretization

Let $\mathcal{T}_h = \cup_e U^e$ be a triangulation of U composed of elements U^e . We use Q^1 (bilinear) finite elements, and we denote by $\{\mathbf{s}_l\}_{l=1}^M$ the nodes of the mesh, and by $\{\phi_l(\mathbf{s})\}_{l=1}^M$ the Lagrangian basis functions. We denote the time-dependent physical positions of the nodes of the Lagrangian mesh by $\{\boldsymbol{\chi}_l(t)\}_{l=1}^M$. Using the Lagrangian basis functions, we define an approximation to $\boldsymbol{\chi}(\mathbf{s}, t)$ by

$$\boldsymbol{\chi}_h(\mathbf{s}, t) = \sum_{l=1}^M \boldsymbol{\chi}_l(t) \phi_l(\mathbf{s}). \quad (23)$$

Because we use interpolatory FE basis functions, $\boldsymbol{\chi}_h(\mathbf{s}_l, t) = \boldsymbol{\chi}_l(t)$. An approximation to the deformation gradient is given by

$$\mathbb{F}_h(\mathbf{s}, t) = \frac{\partial}{\partial \mathbf{s}} \boldsymbol{\chi}_h(\mathbf{s}, t) = \sum_{l=1}^M \boldsymbol{\chi}_l(t) \frac{\partial}{\partial \mathbf{s}} \phi_l(\mathbf{s}). \quad (24)$$

Using $\mathbb{F}_h(\mathbf{s}, t)$, we compute directly $\mathbb{P}_h^e(\mathbf{s}, t)$ and $\mathbf{T}_h(\mathbf{s}, t)$, approximations to the first Piola-Kirchhoff stress tensor and the Lagrangian transmission force density, respectively. For C^0 Lagrangian basis functions, $\boldsymbol{\chi}_h(\mathbf{s}, t)$ is a continuous function of \mathbf{s} , but $\mathbb{F}_h(\mathbf{s}, t)$ is generally discontinuous at internal element boundaries. Hence, \mathbb{P}_h^e and \mathbf{T}_h are also generally only piecewise continuous.

We approximate the Lagrangian force densities $\mathbf{F}(\mathbf{s}, t)$ and $\mathbf{G}(\mathbf{s}, t)$ by

$$\mathbf{F}_h(\mathbf{s}, t) = \sum_{l=1}^M \mathbf{F}_l(t) \phi_l(\mathbf{s}), \text{ and} \quad (25)$$

$$\mathbf{G}_h(\mathbf{s}, t) = \sum_{l=1}^M \mathbf{G}_l(t) \phi_l(\mathbf{s}), \quad (26)$$

where the nodal values $\{\mathbf{F}_l\}_{l=1}^M$ and $\{\mathbf{G}_l\}_{l=1}^M$ must be determined from $\mathbb{P}_h^e(\mathbf{s}, t)$. By restricting the test functions to be linear combinations of the Lagrangian basis functions, we have that Eq. (11) becomes, after rearranging terms,

$$\sum_{l=1}^M \left(\int_U \phi_l(\mathbf{s}) \phi_m(\mathbf{s}) \, d\mathbf{s} \right) \mathbf{F}_l(t) = - \int_U \mathbb{P}_h^e(\mathbf{s}, t) \nabla_{\mathbf{s}} \phi_m(\mathbf{s}) \, d\mathbf{s}, \quad (27)$$

for each $m = 1, \dots, M$. Similarly, Eq. (18) becomes

$$\begin{aligned} \sum_{l=1}^M \left(\int_U \phi_l(\mathbf{s}) \phi_m(\mathbf{s}) \, d\mathbf{s} \right) \mathbf{G}_l(t) &= - \int_U \mathbb{P}_h^e(\mathbf{s}, t) \nabla_{\mathbf{s}} \phi_m(\mathbf{s}) \, d\mathbf{s} \\ &+ \int_{\partial U} \mathbb{P}_h^e(\mathbf{s}, t) \mathbf{N}(\mathbf{s}) \phi_m(\mathbf{s}) \, dA(\mathbf{s}), \end{aligned} \quad (28)$$

for each $m = 1, \dots, M$.

Letting $[\mathbf{F}]$ denote the vector of nodal coefficients of \mathbf{F}_h , we write Eq. (27) as

$$[\mathcal{M}] [\mathbf{F}] = [\mathbf{B}], \quad (29)$$

where $[\mathcal{M}]$ is the so-called consistent mass matrix, which has entries of the form $\int_U \phi_l(\mathbf{s}) \phi_m(\mathbf{s}) \, d\mathbf{s}$. Eq. (28) may be rewritten similarly. The mass matrix $[\mathcal{M}]$ can also be used to evaluate the L^2 inner product of Lagrangian functions on U . In particular, for any $\mathbf{U}_h(\mathbf{s}, t) = \sum_l \mathbf{U}_l(t) \phi_l(\mathbf{s})$ and $\mathbf{V}_h(\mathbf{s}, t) = \sum_l \mathbf{V}_l(t) \phi_l(\mathbf{s})$,

$$(\mathbf{U}_h, \mathbf{V}_h)_s = [\mathbf{U}]^T [\mathcal{M}] [\mathbf{V}]. \quad (30)$$

Different choices of mass matrices (e.g., lumped mass matrices) induce different discrete inner products on U .

To simplify notation, in the remainder of this paper, we drop the subscript “ h ” from our numerical approximations to the Lagrangian variables.

3.3 Lagrangian-Eulerian interaction

As in the conventional IB method, we approximate the singular delta function kernel appearing in the Lagrangian-Eulerian interaction equations by a smoothed two-dimensional Dirac delta function $\delta_h(\mathbf{x})$ that is of the tensor-product form $\delta_h(\mathbf{x}) = \delta_h(x_1) \delta_h(x_2)$. In this work, we take the one-dimensional smoothed delta function $\delta_h(x)$ to be the four-point delta function of Peskin [3].

To compute an approximation to $\mathbf{f} = (f_1, f_2)$ on the Cartesian grid, we construct for each element $U^e \in \mathcal{T}_h$ a Gaussian quadrature rule with N^e quadrature points $\mathbf{s}_Q^e \in U^e$ and weights ω_Q^e , $Q = 1, \dots, N^e$. We then compute f_1 and f_2 on the edges of the Cartesian grid cells via

$$(f_1)_{i-\frac{1}{2}, j} = \sum_{U^e \in \mathcal{T}_h} \sum_{Q=1}^{N^e} F_1(\mathbf{s}_Q^e, t) \delta_h(\mathbf{x}_{i-\frac{1}{2}, j} - \boldsymbol{\chi}(\mathbf{s}_Q^e, t)) \omega_Q^e, \quad \text{and} \quad (31)$$

$$(f_2)_{i, j-\frac{1}{2}} = \sum_{U^e \in \mathcal{T}_h} \sum_{Q=1}^{N^e} F_2(\mathbf{s}_Q^e, t) \delta_h(\mathbf{x}_{i, j-\frac{1}{2}} - \boldsymbol{\chi}(\mathbf{s}_Q^e, t)) \omega_Q^e, \quad (32)$$

where $\mathbf{F}(\mathbf{s}, t) = (F_1(\mathbf{s}, t), F_2(\mathbf{s}, t))$. We use the shorthand

$$\mathbf{f} = \mathcal{S} \mathbf{F}, \quad (33)$$

where $\mathcal{S} = \mathcal{S}(\boldsymbol{\chi})$ is the *force-prolongation operator* implicitly defined by Eqs. (31) and (32).

A corresponding *velocity-restriction operator* $\mathcal{R} = \mathcal{R}(\boldsymbol{\chi})$ is used to determine the motion of the nodes of the Lagrangian mesh from the Cartesian grid velocity field via

$$\frac{d\boldsymbol{\chi}}{dt} = \mathcal{R} \mathbf{u}. \quad (34)$$

There are many possible ways to construct \mathcal{R} ; however, we have found that an effective approach is to require $\frac{d\boldsymbol{\chi}}{dt} = \mathcal{R} \mathbf{u}$ to satisfy the discrete power identity,

$$\left(\mathbf{F}, \frac{d\boldsymbol{\chi}}{dt} \right)_{\mathbf{s}} = (\mathbf{f}, \mathbf{u})_{\mathbf{x}}, \quad (35)$$

which implies that the semi-discrete unified formulation conserves energy during Lagrangian-Eulerian interaction [3]. This power identity can be rewritten as

$$(\mathbf{F}, \mathcal{R} \mathbf{u})_{\mathbf{s}} = (\mathcal{S} \mathbf{F}, \mathbf{u})_{\mathbf{x}}, \quad (36)$$

i.e., $\mathcal{R} = \mathcal{S}^*$.

To construct \mathcal{R} explicitly, it is convenient to use matrix notation. Identifying $[\mathcal{S}]$ and $[\mathcal{R}]$ with the matrix representations of \mathcal{S} and \mathcal{R} , we have that

$$[\mathbf{f}] = [\mathcal{S}] [\mathbf{F}], \text{ and} \quad (37)$$

$$\frac{d[\boldsymbol{\chi}]}{dt} = [\mathcal{R}] [\mathbf{u}]. \quad (38)$$

Eq. (36) then becomes

$$[\mathbf{F}]^T [\mathcal{M}] [\mathcal{R}] [\mathbf{u}] = ([\mathcal{S}] [\mathbf{F}])^T [\mathbf{u}] h^2. \quad (39)$$

If Eq. (39) is to hold for any $[\mathbf{F}]$ and $[\mathbf{u}]$, then $[\mathcal{R}]$ must be defined via

$$[\mathcal{R}] = [\mathcal{M}]^{-1} [\mathcal{S}]^T h^2. \quad (40)$$

In our timestepping scheme, which is stated below in Sec. 4, notice that we need only to apply $[\mathcal{R}]$ to discrete velocity fields defined on the Cartesian grid. Specifically, we do not need to compute $[\mathcal{R}]$ explicitly.

It is straightforward to show that this construction of \mathcal{R} implies that $\frac{d\boldsymbol{\chi}}{dt}(\mathbf{s}, t)$ is an approximation to the L^2 projection of the C^1 Lagrangian vector field

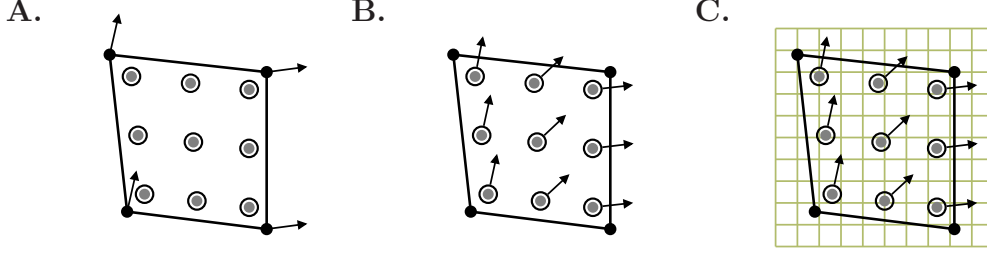


Fig. 2. Prolonging the elastic force density from the Lagrangian mesh onto the Eulerian grid. Starting with an approximation to the force density at the nodes of the Lagrangian mesh (**A**), we use the interpolatory FE basis functions to approximate the force density at quadrature points in the element interior (**B**), and then spread the interpolated forces from the quadrature points to the background Eulerian grid using the smoothed delta function $\delta_h(\mathbf{x})$ (**C**). This approach permits Lagrangian meshes that are significantly coarser than the Eulerian grid so long as the “net” or “submesh” of quadrature points is sufficiently dense. Denser nets of quadrature points can be obtained by increasing the order of the numerical quadrature scheme.

$\mathbf{U}^{\text{IB}}(\mathbf{s}, t) = (U_1^{\text{IB}}(\mathbf{s}, t), U_2^{\text{IB}}(\mathbf{s}, t))$, with

$$U_1^{\text{IB}}(\mathbf{s}, t) = \sum_{i,j} (u_1)_{i-\frac{1}{2},j} \delta_h(\mathbf{x}_{i-\frac{1}{2},j} - \boldsymbol{\chi}(\mathbf{s}, t)) h^2, \text{ and} \quad (41)$$

$$U_2^{\text{IB}}(\mathbf{s}, t) = \sum_{i,j} (u_2)_{i,j-\frac{1}{2}} \delta_h(\mathbf{x}_{i,j-\frac{1}{2}} - \boldsymbol{\chi}(\mathbf{s}, t)) h^2. \quad (42)$$

Because the components of $\mathbf{U}^{\text{IB}}(\mathbf{s}, t)$ are not generally linear combinations of the Lagrangian basis functions, however, generally $\frac{d\mathbf{x}}{dt} \neq \mathbf{U}^{\text{IB}}$.

For the semi-discretized partitioned weak formulation, the value of \mathbf{g} is computed on the Cartesian grid via $\mathbf{g} = \mathcal{S} \mathbf{G}$. The value of \mathbf{t} is computed in a similar manner, but in this case, the numerical integration occurs only over those element boundaries that coincide with ∂U . We use the shorthand $\mathbf{t} = \mathcal{S}^{\partial U} \mathbf{T}$ to denote this operation. We use the same regularized delta function $\delta_h(\mathbf{x})$ to construct both \mathcal{S} and $\mathcal{S}^{\partial U}$. For simplicity, we use the same velocity-restriction operator for both formulations, although with this construction, only the unified formulation will satisfy a discrete power identity. Notice, however, that this choice ensures that the two formulations coincide whenever $\mathbf{T} \equiv 0$.

The Lagrangian-Eulerian interaction operators introduced in this work are different from analogous operators used in standard IB methods. Standard IB methods and schemes such as the IFE method use regularized delta functions to apply nodal forces directly to the Cartesian grid, and to interpolate Cartesian grid velocities directly to the Lagrangian nodes [3]. In such schemes,

$\mathbf{f}(\mathbf{x}, t)$ would be approximated on the Eulerian grid by expressions similar to

$$(f_1^{\text{IB}})_{i-\frac{1}{2},j} = \sum_{l=1}^M (F_1)_l(t) \delta_h(\mathbf{x}_{i-\frac{1}{2},j} - \boldsymbol{\chi}_l(t)) \Delta s_1 \Delta s_2, \text{ and} \quad (43)$$

$$(f_2^{\text{IB}})_{i,j-\frac{1}{2}} = \sum_{l=1}^M (F_2)_l(t) \delta_h(\mathbf{x}_{i,j-\frac{1}{2}} - \boldsymbol{\chi}_l(t)) \Delta s_1 \Delta s_2. \quad (44)$$

In this approach, each nodal force \mathbf{F}_l is applied only to Cartesian grid cells within the support of $\delta_h(\mathbf{x} - \boldsymbol{\chi}_l)$, and the Lagrangian mesh must therefore be finer than the Cartesian grid to avoid “leaks” [3]. The corresponding approach to velocity restriction used by such methods would be to set $\frac{d\boldsymbol{\chi}_l}{dt}$ to equal $\mathbf{U}^{\text{IB}}(\mathbf{s}_l, t)$.

Our force-prolongation operator can be seen as the composition of two operations: first, the nodal values of \mathbf{F} are interpolated from the mesh nodes to a “net” or “submesh” quadrature points within each element; then, $\delta_h(\mathbf{x})$ is used to spread those interpolated force densities from the quadrature points to the Cartesian grid. See Fig. 2. Velocity restriction is similar. First, the Cartesian velocity field is interpolated to the quadrature points using $\delta_h(\mathbf{x})$; these “sampled” values are then used to compute the right-hand-side of an L^2 -projection equation, and the solution of this projection equation determines $\frac{d\boldsymbol{\chi}}{dt}$. In our approach, the Lagrangian structure is watertight so long as the net of quadrature points is sufficiently dense. Denser nets of quadrature points can be obtained by increasing the order of the quadrature rule. In our numerical tests, we use Gaussian quadrature rules that provide approximately nine quadrature points per Cartesian grid cell to construct \mathcal{S} and \mathcal{R} .

4 Temporal discretization

4.1 Basic timestepping scheme

Let $\boldsymbol{\chi}^n$, \mathbf{u}^n , and $p^{n-\frac{1}{2}}$ denote the approximations to the values of $\boldsymbol{\chi}$ and \mathbf{u} at time t^n , and to the value of p at time $t^{n-\frac{1}{2}}$, respectively. We advance the solution values forward in time by the time interval Δt as follows. First, we determine a preliminary approximation to the deformed structure configuration at time t^{n+1} via

$$\frac{\tilde{\boldsymbol{\chi}}^{n+1} - \boldsymbol{\chi}^n}{\Delta t} = \mathcal{R}^n \mathbf{u}^n, \quad (45)$$

where $\mathcal{R}^n = \mathcal{R}(\boldsymbol{\chi}^n)$, and we define an approximation to $\boldsymbol{\chi}$ at time $t^{n+\frac{1}{2}}$ by

$$\boldsymbol{\chi}^{n+\frac{1}{2}} = \frac{\tilde{\boldsymbol{\chi}}^{n+1} + \boldsymbol{\chi}^n}{2}. \quad (46)$$

Then, we solve

$$\rho \left(\frac{\mathbf{u}^{n+1} - \mathbf{u}^n}{\Delta t} + \mathbf{A}^{n+\frac{1}{2}} \right) = -\nabla_h p^{n+\frac{1}{2}} + \mu \nabla_h^2 \frac{\mathbf{u}^{n+1} + \mathbf{u}^n}{2} + \mathbf{f}^{n+\frac{1}{2}}, \quad (47)$$

$$\nabla_h \cdot \mathbf{u}^{n+1} = 0, \quad (48)$$

$$\mathbf{f}^{n+\frac{1}{2}} = \mathcal{S}(\chi^{n+\frac{1}{2}}) \mathbf{F}(\chi^{n+\frac{1}{2}}), \quad (49)$$

$$\frac{\chi^{n+1} - \chi^n}{\Delta t} = \mathcal{R}(\chi^{n+\frac{1}{2}}) \frac{\mathbf{u}^{n+1} + \mathbf{u}^n}{2}, \quad (50)$$

for χ^{n+1} , \mathbf{u}^{n+1} , and $p^{n+\frac{1}{2}}$, where $\mathbf{A}^{n+\frac{1}{2}} = \frac{3}{2}\mathbf{u}^n \cdot \nabla_h \mathbf{u}^n - \frac{1}{2}\mathbf{u}^{n-1} \cdot \nabla_h \mathbf{u}^{n-1}$ is computed via a PPM-type approximation to the nonlinear advection term [30,31]. The timestepping scheme for the partitioned weak formulation is analogous. Notice that solving Eqs. (47)–(50) for χ^{n+1} , \mathbf{u}^{n+1} , and $p^{n+\frac{1}{2}}$ requires the solution of a Crank-Nicolson-type discretization of the time-dependent incompressible Stokes equations. We solve this system of equations via the flexible GMRES (FGMRES) algorithm [34], using \mathbf{u}^n and $p^{n-\frac{1}{2}}$ as initial approximations to \mathbf{u}^{n+1} and $p^{n+\frac{1}{2}}$, and using a pressure-free projection method with multigrid subdomain solvers as a preconditioner [31].

4.2 Initial timestep

Because timestep-lagged values of \mathbf{u} and p are used by the timestepping scheme of Sec. 4.1, we cannot use that scheme for the initial timestep. Instead, we use a two-step predictor-corrector method for $n = 0$. First, we solve

$$\rho \left(\frac{\tilde{\mathbf{u}}^{n+1} - \mathbf{u}^n}{\Delta t} + \mathbf{A}^n \right) = -\nabla_h \tilde{p}^{n+\frac{1}{2}} + \mu \nabla_h^2 \frac{\tilde{\mathbf{u}}^{n+1} + \mathbf{u}^n}{2} + \mathbf{f}^n, \quad (51)$$

$$\nabla_h \cdot \tilde{\mathbf{u}}^{n+1} = 0, \quad (52)$$

$$\mathbf{f}^n = \mathcal{S}(\chi^n) \mathbf{F}(\chi^n), \quad (53)$$

$$\frac{\tilde{\chi}^{n+1} - \chi^n}{\Delta t} = \mathcal{R}(\chi^n) \mathbf{u}^n, \quad (54)$$

for $\tilde{\chi}^{n+1}$, $\tilde{\mathbf{u}}^{n+1}$, and $\tilde{p}^{n+\frac{1}{2}}$, where $\mathbf{A}^n = \mathbf{u}^n \cdot \nabla_h \mathbf{u}^n$. Because we do not have an initial value for the pressure, we use $p = 0$ as an initial guess for $p^{n+\frac{1}{2}}$. Next, we set

$$\chi^{n+\frac{1}{2}} = \frac{\tilde{\chi}^{n+1} + \chi^n}{2} \quad (55)$$

and solve Eqs. (47)–(50) for χ^{n+1} , \mathbf{u}^{n+1} , and $p^{n+\frac{1}{2}}$, except that we use $\mathbf{A}^{n+\frac{1}{2}} = \mathbf{u}^{n+\frac{1}{2}} \cdot \nabla_h \mathbf{u}^{n+\frac{1}{2}}$ with $\mathbf{u}^{n+\frac{1}{2}} = \frac{1}{2}(\tilde{\mathbf{u}}^{n+1} + \mathbf{u}^n)$.

5 Implementation

This version of the IB method is implemented in the open-source IBAMR software [29], a C++ framework for developing fluid-structure interaction models that use the IB method. IBAMR provides support for distributed-memory parallelism and adaptive mesh refinement (AMR). IBAMR relies upon the SAMRAI [35–37], PETSc [38–40], *hypre* [41,42], and `libMesh` [43,44] libraries for much of its functionality.

6 Numerical results

6.1 Thick elliptical shell

This set of numerical tests uses a thick elliptical shell like that employed in the context of the conventional IB method [18, 28] and the fully variational IB method [26] to demonstrate that the IB method can obtain higher-order convergence rates for certain problems. In these computations, the physical domain is $\Omega = [0, 1] \times [0, 1]$ with periodic boundary conditions, and, following Boffi et al. [26], the Lagrangian coordinate domain is $U = [0, 2\pi R] \times [0, w]$, with $R = 0.25$ and $w = 0.0625$, and with periodic boundary conditions in the s_1 direction. The coordinate mapping $\chi : (U, t) \mapsto \Omega$ is given at time $t = 0$ by

$$\chi(\mathbf{s}, 0) = (\cos(s_1/R)(R + s_2) + 0.5, \sin(s_1/R)(R + \gamma + s_2) + 0.5). \quad (56)$$

We use $\gamma = 0$ for static problems and $\gamma = 0.1$ for dynamic problems. In either case, we discretize Ω using an N -by- N Cartesian grid, and we discretize U using a $28M$ -by- M mesh of bilinear (Q^1) elements, with $M = \frac{1}{M_{\text{fac}}} \frac{N}{16}$. The Lagrangian discretization is constructed so that the nodes of the Lagrangian mesh are physically separated by a distance of approximately $M_{\text{fac}}\Delta x$. Representative numerical results are shown in Fig. 3.

6.1.1 Anisotropic shell

We first consider an idealized anisotropic shell that is defined in terms of the strain-energy functional [26],

$$W^e(\mathbb{F}) = \frac{\mu^e}{2w} \left\| \frac{\partial \chi}{\partial s_1}(\mathbf{s}, t) \right\|^2 = \frac{\mu^e}{2w} \mathbb{F}_{\alpha 1} \mathbb{F}_{\alpha 1}, \quad (57)$$

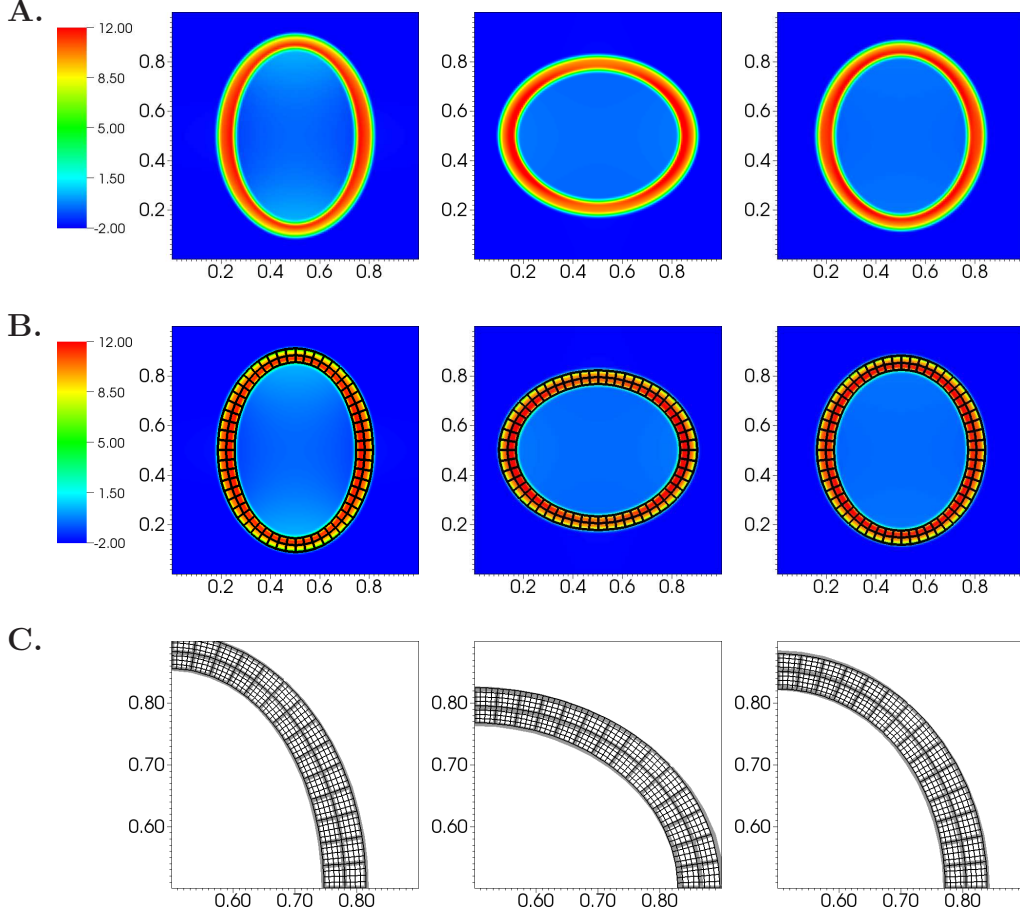


Fig. 3. Representative results from the dynamic ($\gamma = 0.1$) version of the orthotropic shell problem of Sec. 6.1.2 for $N = 128$ and the partitioned (split) weak formulation over the time interval $0 \leq t \leq 1.25$. The computed pressure and structure deformation for $M_{\text{fac}} = 4$ are shown in **A** and **B**. The computed deformations obtained with $M_{\text{fac}} = 1$ and $M_{\text{fac}} = 4$ are compared in **C**. Notice the high level of agreement between the computed deformations in **C**.

where repeated indices imply summation, and for which

$$\mathbb{P}^e(\mathbf{s}, t) = \frac{\partial W^e}{\partial \mathbb{F}}(\mathbf{s}, t) = \frac{\mu^e}{w} \begin{pmatrix} \frac{\partial \chi_1}{\partial s_1} & 0 \\ \frac{\partial \chi_2}{\partial s_1} & 0 \end{pmatrix} = \frac{\mu^e}{w} \begin{pmatrix} \mathbb{F}_{11} & 0 \\ \mathbb{F}_{21} & 0 \end{pmatrix}. \quad (58)$$

This energy functional and stress tensor correspond to an idealized anisotropic elastic material composed of a continuous family of extension-resistant fibers that wrap the thick shell. Because U is periodic in the s_1 direction, $\mathbb{P}^e \mathbf{N} \equiv 0$ along ∂U . This reflects the fact that none of the fibers terminate along the boundary of the structure. Because the transmission force vanishes in this case, the unified and partitioned weak formulations are identical.

When we set $\gamma = 0$, the initial configuration of the elastic shell is an equilib-

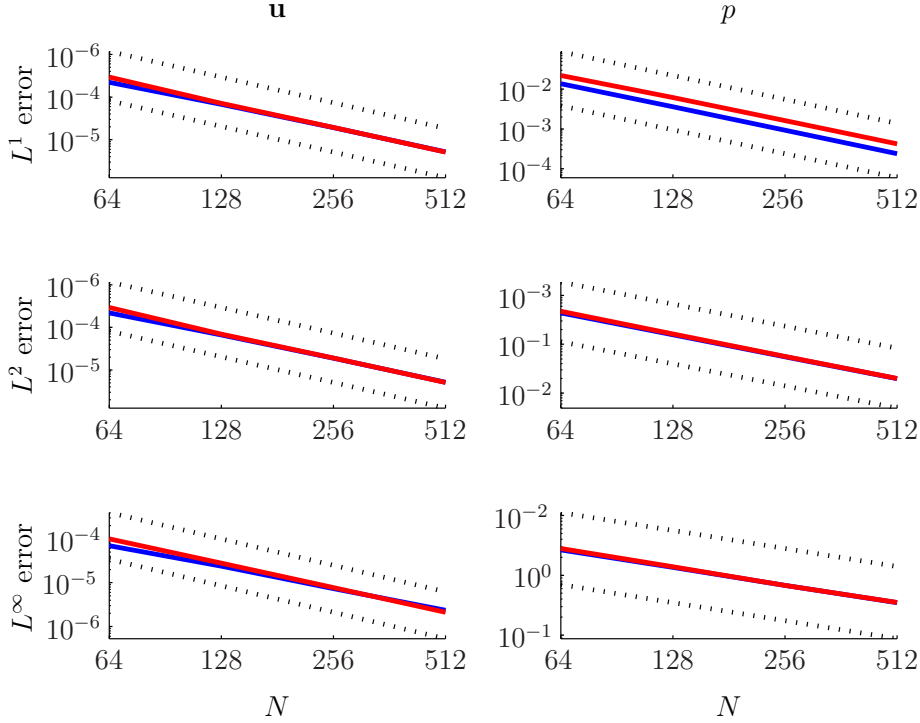


Fig. 4. Errors in \mathbf{u} and p in discrete L^1 , L^2 , and L^∞ norms for the static ($\gamma = 0$) version of the idealized anisotropic shell problem of Sec. 6.1.1. Errors for $M_{\text{fac}} = 1$ are plotted in blue, and errors for $M_{\text{fac}} = 4$ are plotted in red. Reference lines with slope -2 are provided for the \mathbf{u} error data. For p , reference lines with slopes -2, -1.5, and -1 are provided for the L^1 , L^2 , and L^∞ norm data, respectively.

rium configuration of the continuous problem, so that $\mathbf{u}(\mathbf{x}, t) \equiv 0$. Requiring $\int_{\Omega} p(\mathbf{x}, t) d\mathbf{x} = 0$, it can be shown [26] that

$$p(\mathbf{x}, t) = \begin{cases} p_0 + \frac{\mu^e}{R} & r \leq R, \\ p_0 + \frac{\mu^e}{w} \frac{1}{R} (R + w - r) & R < r \leq R + w, \\ p_0 & R + w < r, \end{cases} \quad (59)$$

where $r = \|\mathbf{x} - (0.5, 0.5)\|$ and $p_0 = \frac{\pi\mu^e}{3w} \left(R^2 - \frac{(R+w)^3}{R} \right)$. We set $\rho = 1$, $\mu = 1$, and $\mu^e = 1$, and we consider the time interval $0 \leq t \leq 3$. Fig. 4 summarizes the error data at time $t = 3$ for $N = 64, 128, 256$, and 512 and $M_{\text{fac}} = 1$ and 4 , with $\Delta t = 0.25\Delta x$. Second-order convergence rates are observed in the discrete L^1 , L^2 , and L^∞ norms for the velocity field. Second-order convergence rates are also observed for the pressure in the discrete L^1 norm; however, because the pressure field is C^0 but not C^1 , only first-order convergence rates are observed for the pressure in the discrete L^∞ norm, and intermediate convergence rates are observed in the L^2 norm.

We also consider the case in which $\gamma = 0.1$, so that the initial configuration of the shell is not in equilibrium. We set $\rho = 1$, $\mu = 0.01$, and $\mu^e = 1$, yielding a Reynolds number of approximately 50. We consider the time interval

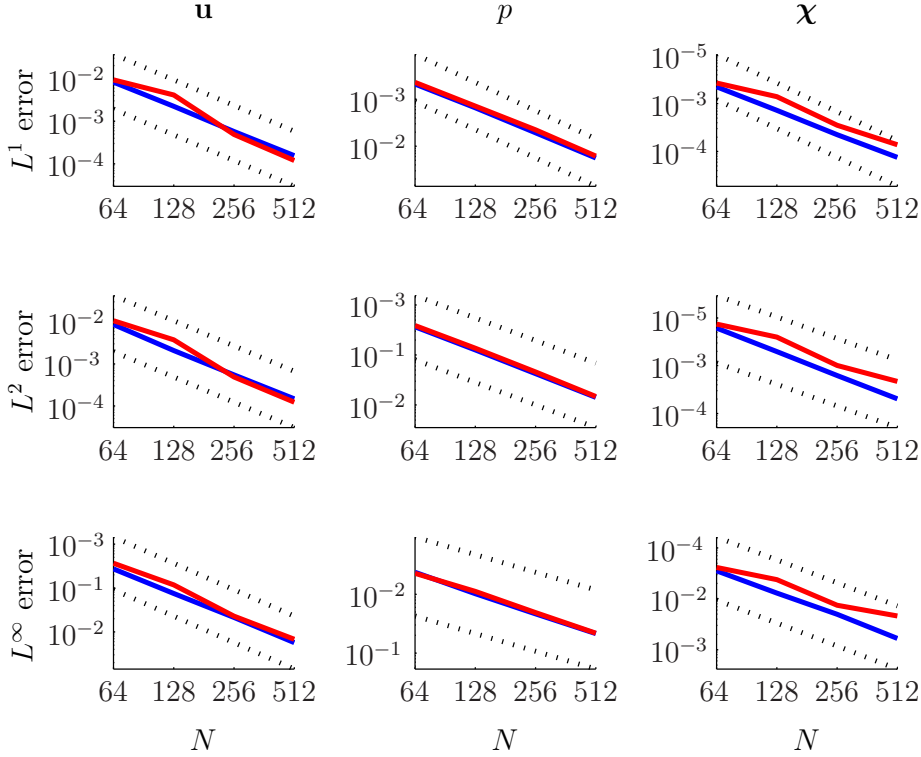


Fig. 5. Errors in \mathbf{u} , p , and χ in discrete L^1 , L^2 , and L^∞ norms for the dynamic ($\gamma = 0.1$) version of the idealized anisotropic shell problem of Sec. 6.1.1. Errors for $M_{\text{fac}} = 1$ are plotted in blue, and errors for $M_{\text{fac}} = 4$ are plotted in red. Reference lines with slope -2 are provided for the \mathbf{u} error data. For p , reference lines with slopes -2 , -1.5 , and -1 are provided for the L^1 , L^2 , and L^∞ norm data, respectively. For χ , reference lines with slope -2 are provided for the L^1 norm data, and lines with slopes -1.5 are provided for the L^2 and L^∞ norm data.

$0 \leq t \leq 0.75$, which corresponds to approximately one damped oscillation of the shell. Fig. 5 summarizes the error data at time $t = 0.75$ for $N = 64, 128, 256,$ and 512 and $M_{\text{fac}} = 1$ and 4 , with $\Delta t = 0.25\Delta x$. Essentially second-order convergence rates are observed in the discrete L^1 , L^2 , and L^∞ norms for the velocity field. Essentially second-order convergence rates are also observed for the pressure in the discrete L^1 norm, whereas only first-order convergence is observed in the L^∞ norm, and intermediate convergence rates are observed in the L^2 norm. Convergence rates for the deformation are somewhat less regular, with nearly second-order convergence rates being observed in the discrete L^1 norm and between first- and second-order convergence rates observed in the discrete L^2 and L^∞ norms.

Notice that in all cases, accuracy is largely similar for both choices of M_{fac} , suggesting that the scheme yields results that are largely independent of the relative coarseness of the Lagrangian mesh. In particular, these results suggest that the scheme does not allow leaks at fluid-structure interfaces, even for Lagrangian meshes that are extremely coarse compared to the Eulerian grid.

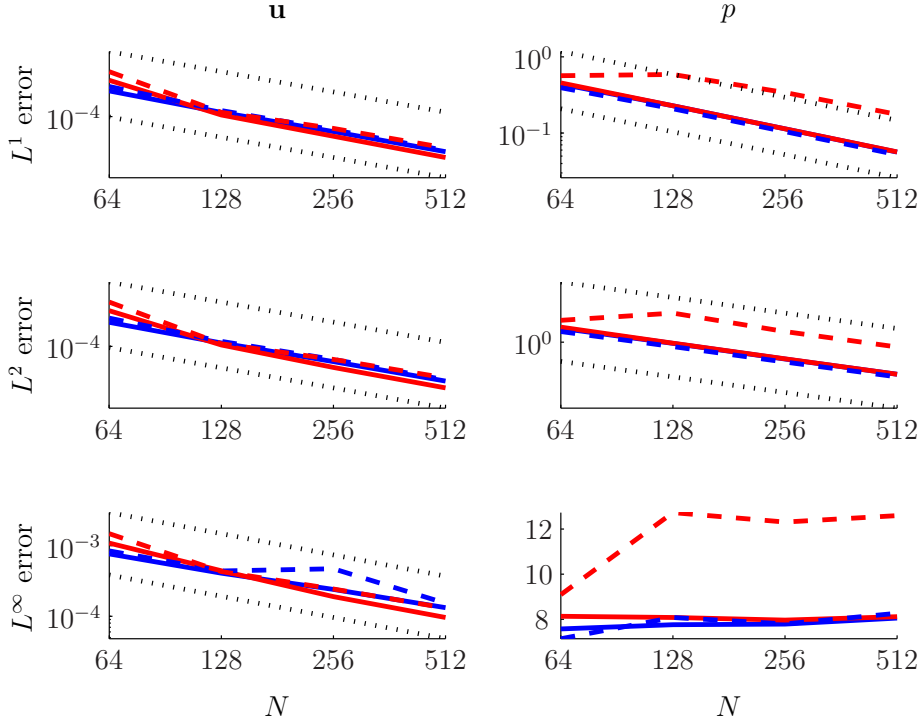


Fig. 6. Errors in \mathbf{u} and p in discrete L^1 , L^2 , and L^∞ norms for the static ($\gamma = 0$) version of the orthotropic shell problem of Sec. 6.1.2. Errors for $M_{\text{fac}} = 1$ are plotted in blue, and errors for $M_{\text{fac}} = 4$ are plotted in red; errors for the partitioned formulation appear as solid lines, and errors for the unified formulation appear as dashed lines. Reference lines with slope -1 are provided for the \mathbf{u} error data. For p , reference lines with slopes -1 and -0.5 are provided for the L^1 and L^2 norm data, respectively.

6.1.2 Orthotropic shell

The second elasticity model that we use for this problem is an orthotropic material model defined in terms of the strain-energy functional [26],

$$W^e(\mathbb{F}) = \frac{\mu^e}{2w} \left(\left\| \frac{\partial \chi}{\partial s_1}(\mathbf{s}, t) \right\|^2 + \left\| \frac{\partial \chi}{\partial s_2}(\mathbf{s}, t) \right\|^2 \right) = \frac{\mu^e}{2w} \mathbb{F} : \mathbb{F}, \quad (60)$$

for which

$$\mathbb{P}^e(\mathbf{s}, t) = \frac{\partial W^e}{\partial \mathbb{F}}(\mathbf{s}, t) = \frac{\mu^e}{w} \mathbb{F}(\mathbf{s}, t). \quad (61)$$

This energy functional and stress tensor correspond to an elastic material composed of two continuous families of fibers. The first family of fibers wraps the elliptical shell circumferentially, and the second family is composed of radial fibers that are orthogonal to the circumferential fibers. Because one family of fibers terminates along the fluid-structure interfaces, there is a singular force layer along $\partial \chi(U, t)$ that must be balanced by discontinuities in the pressure and viscous stress. Therefore, in this case the discretized unified and partitioned formulations yield different results.

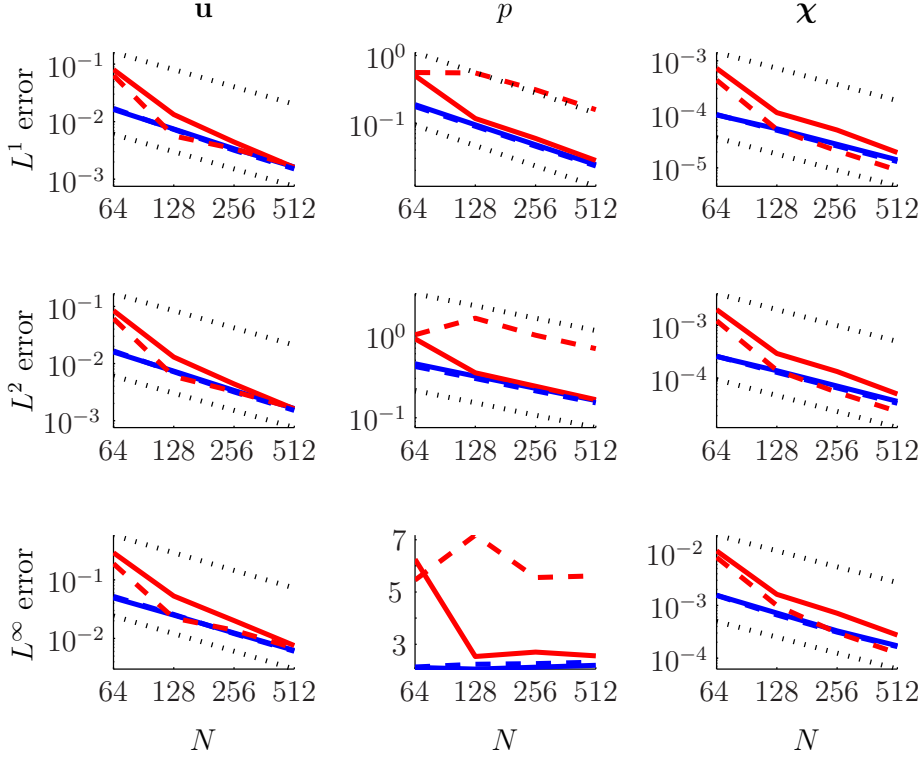


Fig. 7. Errors in \mathbf{u} , p , and χ in discrete L^1 , L^2 , and L^∞ norms for the dynamic ($\gamma = 0.1$) version of the orthotropic shell problem of Sec. 6.1.2. Errors for $M_{\text{fac}} = 1$ are plotted in blue, and errors for $M_{\text{fac}} = 4$ are plotted in red; errors for the partitioned formulation appear as solid lines, and errors for the unified formulation appear as dashed lines. Reference lines with slope -1 are provided for the \mathbf{u} error data. For p , reference lines with slopes -1 and -0.5 are provided for the L^1 and L^2 norm data, respectively. For χ , reference lines with slope -1 are provided.

We first set $\gamma = 0$, which is an equilibrium configuration of the continuous problem, so that $\mathbf{u}(\mathbf{x}, t) \equiv 0$. Requiring $\int_{\Omega} p(\mathbf{x}, t) \, d\mathbf{x} = 0$, it can be shown [26] that

$$p(\mathbf{x}, t) = \begin{cases} p_0 + \mu^e \left(\frac{1}{R} - \frac{1}{R+w} \right) & r \leq R, \\ p_0 + \frac{\mu^e}{w} \left(\frac{1}{R} (R+w-r) + \frac{R}{R+w} \right) & R < r \leq R+w, \\ p_0 & R+w < r, \end{cases} \quad (62)$$

with $r = \|\mathbf{x} - (0.5, 0.5)\|$ and $p_0 = \frac{\pi\mu^e}{3w} \left(3wR + R^2 - \frac{(R+w)^3}{R} \right)$. We set $\rho = 1$, $\mu = 1$, and $\mu^e = 1$, and we consider the time interval $0 \leq t \leq 3$. Fig. 6 summarizes the error data at time $t = 3$ for $N = 64, 128, 256$, and 512 and $M_{\text{fac}} = 1$ and 4 , with $\Delta t = 0.25\Delta x$. First-order convergence rates are observed for \mathbf{u} in all norms. First-order convergence rates are also observed for p in the L^1 norm. Because p possesses discontinuities at fluid-structure interfaces for this problem, however, the present method yields convergence rates of 0.5 in the L^2 norm, and does not converge in the L^∞ norm.

We also consider the case in which $\gamma = 0.1$, so that the initial configuration of the shell is not in equilibrium. Because there is no exact analytic solution available for this problem, we estimate the convergence rates in a standard way by computing the norms of the differences of quantities computed on an N -by- N Cartesian grid and corresponding Lagrangian mesh, and those computed on a $2N$ -by- $2N$ Cartesian grid and corresponding Lagrangian mesh. We set $\rho = 1$, $\mu = 0.01$, and $\mu^e = 1$, yielding a Reynolds number of approximately 50. We consider the time interval $0 \leq t \leq 1.25$, which corresponds to approximately one damped oscillation of the shell. Fig. 7 summarize the error data at time $t = 0.75$ for $N = 64, 128, 256, \text{ and } 512$ and $M_{\text{fac}} = 1$ and 4, with $\Delta t = 0.25\Delta x$. Essentially first-order convergence rates are observed for \mathbf{u} and $\boldsymbol{\chi}$ in all norms, whereas p exhibits first-order convergence in only the L^1 norm.

For this problem, we find that the unified and partitioned formulations yield similar accuracy in most cases for \mathbf{u} , and that the unified formulation can offer modestly better accuracy for $\boldsymbol{\chi}$. By contrast, the partitioned formulation offers significantly better accuracy for the pressure for relatively coarse Lagrangian meshes. This property appears also to result in improvements in volume conservation; see Sec. 6.2.

6.2 Soft elastic disc

These tests demonstrate the volume-conservation properties of our method by considering the problem of a soft elastic disc immersed in a lid-driven cavity flow. The physical domain is $\Omega = [0, 1]^2$, and the physical boundary conditions are $\mathbf{u} \equiv 0$ along the left ($x_1 = 0$), right ($x_1 = 1$), and bottom ($x_2 = 0$) boundaries of Ω , and $\mathbf{u} \equiv (1, 0)$ along the top ($x_2 = 1$) boundary of Ω . The immersed structure is a disc of radius 0.2 that is initially centered about the position $(0.6, 0.5)$. The physical domain is discretized on an $N \times N$ Cartesian grid, and the Lagrangian coordinate domain is discretized using a semistructured mesh of bilinear (Q^1) elements that is constructed so that the coarsest element is approximately a factor of M_{fac} coarser than the background Eulerian grid. Near $\partial\Omega$, we use a modified regularized delta function formulation [19] to ensure that force and torque are conserved and that velocity is interpolated accurately during Lagrangian-Eulerian interaction.

We use an isotropic neo-Hookean material model

$$W^e(\mathbb{F}) = \frac{\mu^e}{2} \mathbb{F} : \mathbb{F}, \quad (63)$$

for which

$$\mathbb{P}^e(\mathbf{s}, t) = \mu^e \mathbb{F}. \quad (64)$$

Because generally $\mathbb{P}^e \mathbf{N} \neq 0$, the solution will generally possess discontinuities

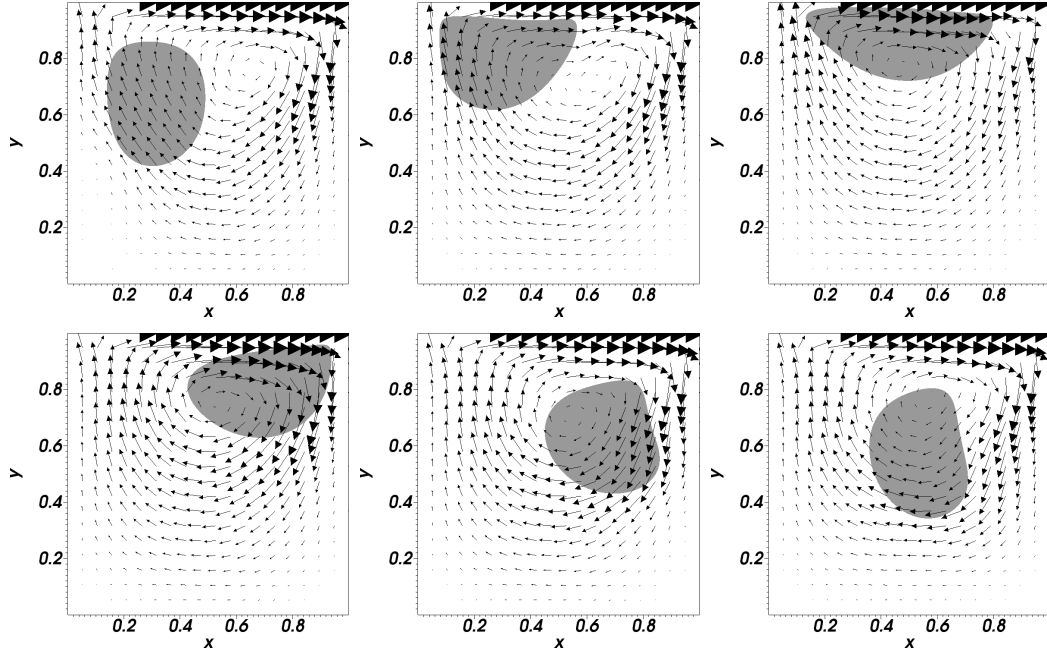


Fig. 8. Results from the elastic disc problem of Sec. 6.2 shown at equally spaced times during the interval $3 \leq t \leq 8$.

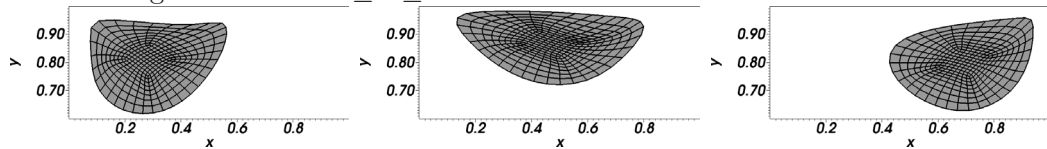


Fig. 9. Similar to Fig. 8, but here showing an enlarged view of the structure at times $t = 4, 5,$ and 6 .

in the pressure and viscous stress at fluid-structure interfaces, and we expect the IB method to yield no better than first-order convergence rates for this example. Notice also that this problem possesses well-known corner singularities that also act to reduce the convergence rate of the scheme. Although it is possible to devise numerical schemes that accurately treat the corner singularities present in the classical lid-driven cavity flow [45], we do not employ such a method in this work.

As in previous studies of this problem [46, 47], we set $\mu = 0.01$, $\rho = 1$, and $\mu^e = 0.1$. The initial velocity is $\mathbf{u} \equiv 0$, and the initial deformation is $\chi(\mathbf{s}, 0) \equiv \mathbf{s}$. We consider the time interval $0 \leq t \leq 10$, during which the disc is subjected to slightly more than one rotation. The structure becomes entrained in the shearing flow along the cavity lid from $t \approx 4$ until $t \approx 6$, and during this time is subjected to very large deformations. Sample results are shown in Figs. 8 and 9. Fig. 10 shows the relative change in disc area for different values of N and M_{fac} . Over this time interval, the maximum area change yielded by the unified formulation is less than 0.5% for $N = 64$ and $M_{\text{fac}} = 4$, and is approximately 0.2% for $N = 64$ and $M_{\text{fac}} = 1$. For the partitioned formulation,

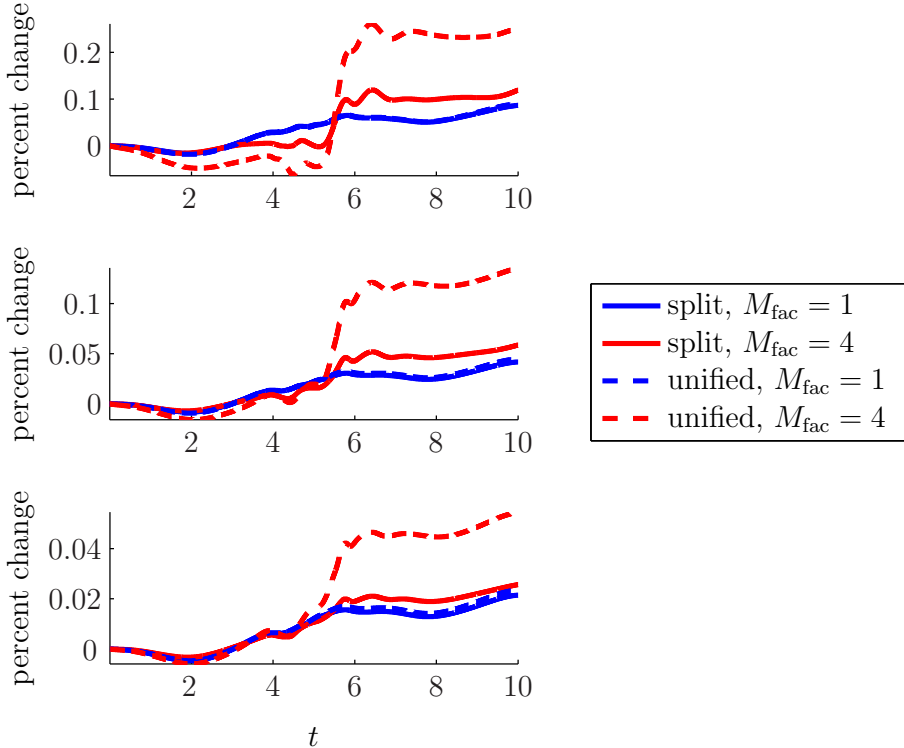


Fig. 10. Percent change in area as a function of time for the elastic disc problem. Results are shown for the unified and partitioned formulations for $N = 128, 256,$ and 512 for $M_{\text{fac}} = 1$ and 4 .

the maximum area change approximately than 0.2% for $N = 64$ and both $M_{\text{fac}} = 1$ and $M_{\text{fac}} = 4$. In general, the partitioned formulation appears to use superior volume conservation, and its volume-conservation properties seem to be relatively insensitive to the relative coarseness of the Lagrangian mesh. Using either formulation, volume errors converge to zero at essentially a first-order rate. These results compare favorably to those obtained by the IFE method, which, even for relatively fine Lagrangian meshes, yields volume losses of up to 20% when applied to the same test problem without using a volume-conservation algorithm, and which exhibits volume losses of approximately 2.5% when using a volume-conservation algorithm [47].

6.3 Collapsible channel flow

These tests consider the problem of steady pressure-driven flow in a two-dimensional collapsible channel [48]. The fluid properties are $\rho = 1 \text{ gm/cm}^3$ and $\mu = 0.01 \text{ ba} \cdot \text{s}$. The channel is of length $L = 40 \text{ cm}$ and width $D = 1 \text{ cm}$ and is centered in the region $\Omega = [0, L] \times [0, H]$ with $H = 3D$. In the reference configuration, the channel walls have thicknesses $w = 0.01D$ and are straight. A portion of the upper wall of length $L_f = 5 \text{ cm}$ is flexible, and an upstream portion of the upper wall of length $L_u = 5 \text{ cm}$ and a downstream portion

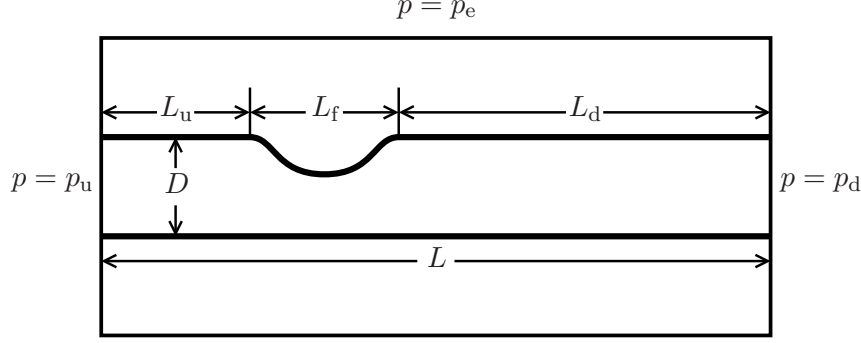


Fig. 11. A partially-collapsible channel of length L and width D . The channel is centered in the region $\Omega = [0, L] \times [0, H]$ with $H = 3D$. A portion of the upper wall of length L_f is flexible, and an upstream portion of the upper wall of length L_u and a downstream portion of length L_d are both rigid. The entire length of the lower wall is also rigid. We set the upstream pressure in the channel to p_u , the downstream pressure to p_d , and the external pressure to p_e .

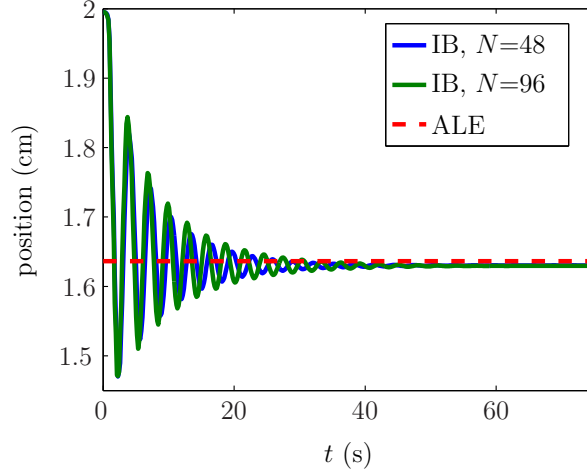


Fig. 12. Trajectory of a material point on the flexible section of the collapsible channel for two different grid resolutions. The y position of material point $\mathbf{s} = (7.5, 2.0)$, which is initially located in the center of the flexible portion of the upper wall, is plotted as a function of time for $N = 48$ and 96 . Although there are differences in the dynamics, notice that the steady-state configurations are the same for both grid spacings.

of length $L_d = 30$ cm are rigid. The entire length of the lower wall is also rigid. The tangential velocity is clamped to zero along $\partial\Omega$. At steady-state, the upstream pressure in the channel is $p_u = 0.45$ Pa, the downstream pressure is $p_d = 0$ Pa, and the external pressure is $p_e = 1.755$ Pa. See Fig. 11. Near $\partial\Omega$, we again use a modified regularized delta function formulation [19] to ensure that force and torque are conserved and that velocity is interpolated accurately during Lagrangian-Eulerian interaction.

In the flexible portion of the wall, we use a St. Venant-Kirchhoff elasticity

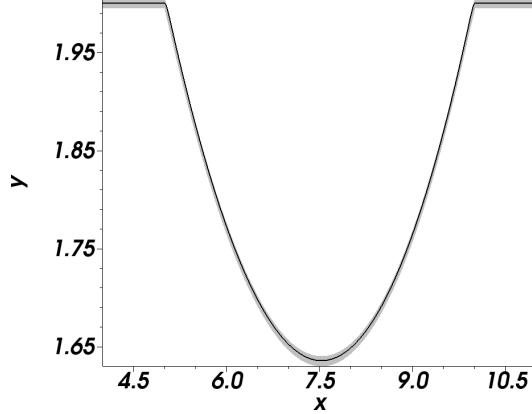


Fig. 13. Comparison between IB and ALE results for the collapsible channel benchmark. The steady-state position of the upper wall in the vicinity of the flexible region is shown as computed by the IB (grey) and ALE (black) methods. Despite the differences between the two schemes, the deformations predicted by both methods are essentially identical.

model, for which

$$W^e = \frac{\lambda^e}{2} \text{tr}(\mathbb{E})^2 + \mu^e \text{tr}(\mathbb{E}^2), \quad (65)$$

where $\mathbb{E} = \frac{1}{2}(\mathbb{C} - \mathbb{I})$ and $\mathbb{C} = \mathbb{F}^T \mathbb{F}$. The constitutive parameters are given by $\mu^e = \frac{1}{2} E^e / (1 + \nu^e)$ and $\lambda^e = (E^e \nu^e) / ((1 + \nu^e)(1 - 2\nu^e))$, in which $E^e = 71.8$ kPa is the Young’s modulus of the material and $\nu^e = 0.45$ is the Poisson ratio. Rigidity constraints are enforced by a feedback-forcing approach, in which

$$\mathbf{F}(\mathbf{s}, t) = \kappa^e(\mathbf{s})(\mathbf{s} - \boldsymbol{\chi}(\mathbf{s}, t)), \quad (66)$$

where $\kappa^e(\mathbf{s}) > 0$ is a penalty parameter. Notice that as $\kappa^e \rightarrow \infty$, $\boldsymbol{\chi}(\mathbf{s}, t) \rightarrow \mathbf{s}$.

We compare the results produced by the unified version of the present IB method to results that were obtained by an arbitrary Lagrangian-Eulerian (ALE) method [48, 49]. There are important differences between the physical problems used by the ALE method and the present IB method. In particular, the IB model treats the channel walls as “thick” incompressible structures, describes the flexible portion of the wall as a viscoelastic material, and considers the channel to be totally immersed in fluid. The ALE scheme treats the channel walls as thin elastic beams and excludes viscous and inertial effects in walls and the region exterior to the channel. Consequently, the dynamics produced by the two methods will generally be different; however, if a set of parameter values yields unique steady-state solutions for both models, the equilibrium solutions yielded by both methods will be essentially identical.

We discretize Ω using an $\frac{L}{H}N$ -by- N Cartesian grid with $N = 48$ and 96, and we discretize each channel wall using a single layer of bilinear elements, each of length Δx and width w ($w \ll \Delta x$) in the reference configuration. We use $\Delta t = 4.05\text{e-}3\Delta x$, and in the rigid portions of the channel walls, we set $\kappa^e =$

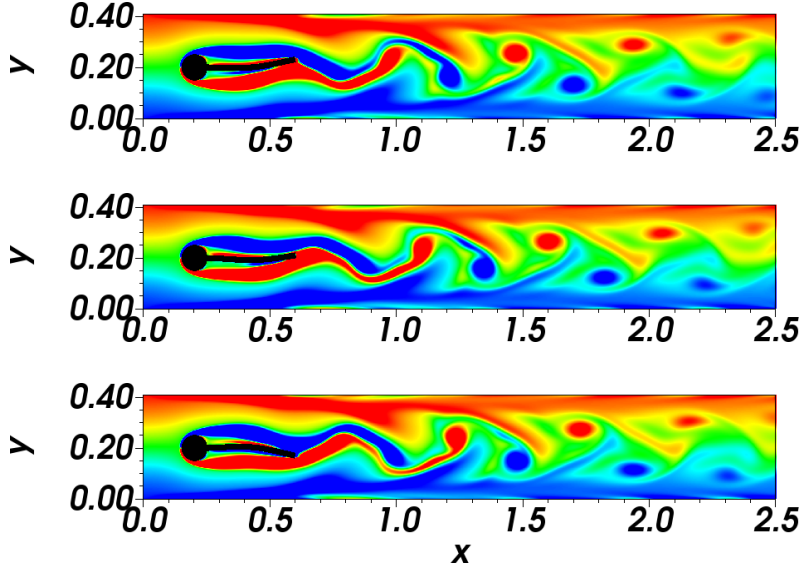


Fig. 14. Sample results from the IB version of the Turek-Hron fluid-structure interaction benchmark problem [50] at $Re = 200$. The fluid vorticity ranges from -30 m/s^2 (blue) to $+30 \text{ m/s}^2$ (red). The structure is shown in black.

$1.0e3\Delta x/\Delta t^2$, which is approximately the largest value of κ^e that is stable for the physical and numerical parameters considered. We increase the driving and loading pressures from zero over a time interval of 1 s. By $t = 100 \text{ s}$ the system has reached equilibrium. At steady state, $Re \approx 80$. The IB method appears to yield converged steady-state deformations for $N = 48$; see Fig. 12. The final configurations generated by the IB and ALE methods are shown in Fig. 13. It can be seen that the deformations generated by the two methods are essentially identical. The maximum y displacements determined by the two methods also agree to within 0.5%: in the IB model, the maximum y displacement of the centerline of the upper wall is 0.3654 cm, whereas in the ALE model, it is 0.3641 cm. Recall that the thickness of the beam is $w = 0.01 \text{ cm}$. Given the differences between the mathematical models and numerical schemes, the agreement between the IB and ALE methods is excellent.

6.4 Turek-Hron fluid-structure interaction benchmark

This section presents preliminary results obtained by our IB method for the Turek-Hron fluid-structure interaction benchmark problem [50], which considers channel flow past a structure composed of a rigid cylinder and a trailing elastic bar; see Fig. 14. We use the version of this problem at $Re = 200$, for which the fluid properties are $\rho = 1000 \text{ kg/m}^3$ and $\mu = 1 \text{ Pa} \cdot \text{s}$, and for which the mass density of the elastic bar is the same as that of the fluid. The channel is $\Omega = [0, L] \times [0, H]$ with $L = 2.5 \text{ m}$ and $H = 0.41 \text{ m}$. No-slip and no-penetration boundary conditions ($\mathbf{u} \equiv 0$) are used along the bottom

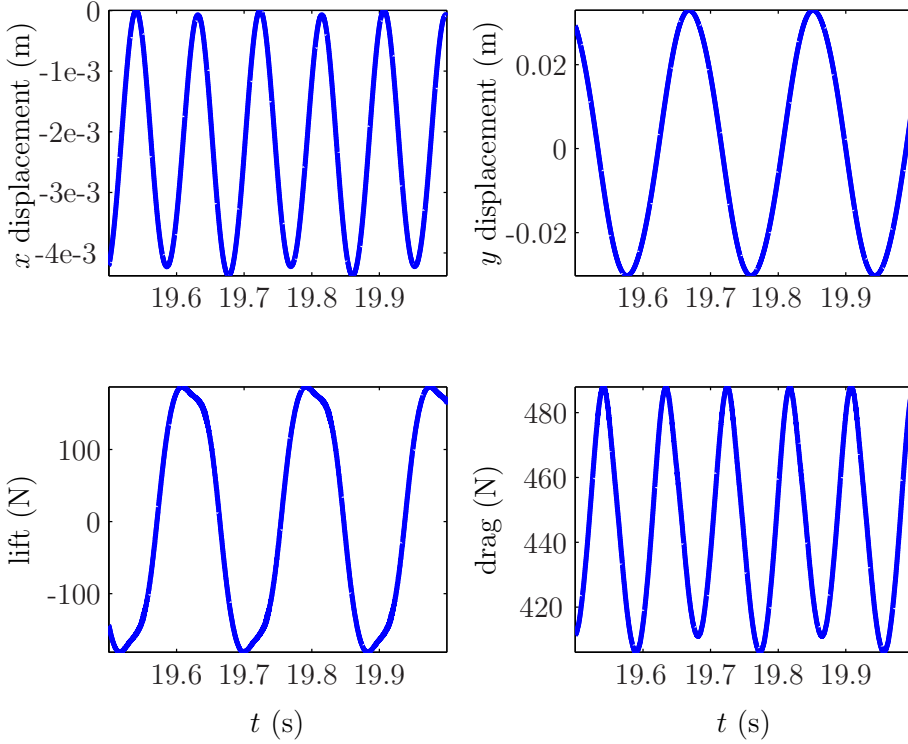


Fig. 15. x and y displacements of the control point A and lift and drag forces for the fluid-structure interaction benchmark problem for $N = 328$.

($x_2 = 0$) and top ($x_2 = H$) boundaries of Ω . A parabolic inflow profile of the form $u_1(x_2, t) = 1.5\bar{U}(t)\frac{y(H-y)}{(H/2)^2}$, with

$$\bar{U}(t) = (2.0 \text{ m/s}) \times \begin{cases} \frac{1}{2}(1 - \cos(\pi t/2)) & \text{if } t < 2, \\ 1 & \text{otherwise,} \end{cases} \quad (67)$$

is imposed along the $x_1 = 0$ boundary, and zero-tangential-slip and zero-normal-traction boundary conditions are imposed at $x_1 = L$.

The disc has center $C = (0.2 \text{ m}, 0.2 \text{ m})$ and radius $R = 0.05 \text{ m}$ and is held rigid via a penalty approach like that used in Sec. 6.3. The elastic bar is attached to the back of the disc and has length $l = 0.35 \text{ m}$ and width $h = 0.02 \text{ m}$. A St. Venant-Kirchhoff model is used to describe the elasticity of the bar with $\mu^e = 2.0\text{e}6 \text{ MPa}$ and $\nu^e = 0.4$. A control point A with initial position $(0.6 \text{ m}, 0.2 \text{ m})$ is attached to the center of the trailing edge of the bar.

There are some differences between the present IB model and the benchmark problem defined by Turek and Hron [50]. In particular, in the original specification, the elastic bar is a compressible hyperelastic material. Because of the form of the material stress tensor used by this IB formulation, however, in the IB version of this problem, the bar is an incompressible viscoelastic material; see Eqs. (1) and (2). The extent to which this problem is sensitive to these

		M_{fac}				conventional
		0.5	1	2	4	IB
	64	0.368	0.156	0.100	0.089	0.312
N	128	1.630	0.649	0.383	0.318	1.525
	256	6.441	2.953	1.762	1.416	6.065

Table 1

Average wall-clock time (in seconds) per timestep for the dynamic version of the problem of Sec. 6.1.2. We also provide timings for a version of this method similar to the standard IB method, in which we use a diagonally-lumped mass matrix, set $M_{\text{fac}} = 0.5$, and use the trapezoidal rule to construct \mathcal{S} and \mathcal{R} .

differences has not yet been characterized. An extension of the present IB method to treat the structure as an elastic, rather than viscoelastic, material seems feasible but has not yet been attempted. Modifying the present method to model the structure as a compressible material appears more difficult.

We discretize Ω using an $\frac{L}{H}N$ -by- N Cartesian grid. The structure is the superposition of a circular disc and an elastic bar, which are both discretized using bilinear elements with edge lengths that are no larger than Δx . We set $\Delta t = 7.8125\text{e-}3\Delta x$ and use $\kappa^e = 1.0\text{e}5\Delta x/\Delta t^2$, which is approximately the largest value of κ^e that is stable for these physical and numerical parameters. Sample results obtained using the unified formulation with $N = 328$ are shown in Figs. 14 and 15. Over the time interval [19.5 s, 20 s], the x displacement of control point A has mean $-2.18\text{e-}3$ m and amplitude $2.19\text{e-}3$ m; the y displacement has mean $1.34\text{e-}3$ m and amplitude $3.16\text{e-}2$ m; the lift force has mean 2.80 N and amplitude $1.84\text{e+}2$ N; and the drag force has mean $4.47\text{e+}2$ N and amplitude 40.9 N. The frequency of the x displacements of A is approximately 11.0/s, and the frequency of the y displacements is approximately 5.4/s. These values are all within the range of results obtained by various other numerical methods that have been applied to this problem [50, 51].

6.5 Timing results

We conclude by presenting preliminary timing data obtained for the dynamic version of the problem of Sec. 6.1.2. For these tests, we perform the first 64 timesteps for various choices of N and M_{fac} using the partitioned version of the method. We also “simulate” the conventional IB method within our implementation by using the unified formulation, using a diagonally-lumped mass matrix, setting $M_{\text{fac}} = 0.5$, and using the trapezoidal rule to construct \mathcal{S} and \mathcal{R} . We record the wall-clock time required using the C function `clock_gettime()` with the `CLOCK_REALTIME` timer. Timings were performed using a single core of a compute server equipped with four quad-core 2.3 GHz AMD Barcelona

CPUs and 32 GB RAM. Results are summarized in Table 1. Notice that larger values of M_{fac} , which correspond to *coarser* Lagrangian meshes, always yield smaller runtimes. Also notice that the Lagrangian-Eulerian interaction operators introduced in this work generally yield better performance than those of the conventional IB approach except for the finest Lagrangian meshes.

We emphasize that we have not yet fully optimized the performance of our implementation of this method; such optimizations could change these timing results significantly. This is especially likely for the simulated version of the conventional IB method, for which there are known optimizations that we have not yet implemented. Nonetheless, these preliminary results suggest that the reductions in the number of Lagrangian degrees of freedom permitted by the novel Lagrangian-Eulerian interaction operators introduced herein can yield significant improvements in runtime.

7 Conclusions

In this paper, we have described a version of the IB method for problems of fluid-structure interaction that uses general elasticity models with unstructured FE discretizations while retaining a Cartesian grid finite difference scheme for the incompressible Navier-Stokes equations. Although we only consider cases in which the elasticity of the structure is described by a hyperelastic constitutive law defined in terms of a strain-energy functional $W^e(\mathbb{F})$, our numerical algorithm does not rely on the availability of such an energy functional and requires only a routine to evaluate the material stress. Consequently, there appears to be no fundamental difficulty in using this method with materials that are described solely in terms of Lagrangian stress tensors.

Our method is based on a strong formulation of the continuous IB equations introduced by Boffi et al. [26]. We consider two different restatements of these equations that each use a weak formulation of the Lagrangian equations of nonlinear elasticity. One of these reformulations treats the internal and boundary stresses within the immersed elastic structure using a single, unified, volumetric elastic force density. The other partitions these stresses into an internal elastic force density supported on the interior of the structure, and a transmission elastic force density supported on fluid-structure interfaces. Both weak formulations are demonstrated to yield similar convergence rates, but the partitioned formulation is seen to yield higher accuracy for Lagrangian meshes that are relatively coarse in comparison to the background Eulerian grid. The partitioned formulation is also seen to yield superior volume conservation in comparison to the unified formulation. A limitation of the partitioned formulation is that it does not satisfy a discrete power identity that implies that energy is conserved during Lagrangian-Eulerian interaction. Such

a power identity is satisfied by the unified formulation, as may be necessary to obtain a stable implicit timestepping scheme [52].

A key contribution of this paper is that it introduces a new approach to Lagrangian-Eulerian interaction that overcomes a longstanding limitation of the IB method, namely the requirement that the Lagrangian mesh be approximately twice as fine as the background Eulerian grid to avoid leaks at fluid-structure interfaces. Numerical examples demonstrate that our scheme permits the use of Lagrangian meshes that are at least four times as coarse as the background Eulerian grid without leak. We speculate that the Lagrangian mesh may be arbitrarily coarse with respect to the background Eulerian grid without leak as long as the numerical quadrature scheme used to discretize the Lagrangian-Eulerian interaction equations has a sufficiently dense net of quadrature points. In two spatial dimensions, our scheme has been demonstrated to reduce the number of Lagrangian degrees of freedom by a factor of at least $8^2 = 64$ in comparison to the conventional IB method; in three spatial dimensions, we expect that we shall be able to see savings on the order of $8^3 = 512$ or more. These reductions in the number of Lagrangian degrees of freedom are also shown to translate into improved wall-clock timings, although these timings were obtained using an implementation of the method that has not yet been fully optimized. Of course, over-coarsening the Lagrangian mesh can result in reduced accuracy. A straightforward generalization of the present approach is to use higher-order FE discretizations, which may permit coarser Lagrangian meshes without sacrificing accuracy.

Finally, we speculate that the partitioned formulation could be useful in constructing higher-order versions of the IB method. In particular, the partitioned formulation is well-suited for developing a hybrid approach in which the IB method is used to treat the volumetric internal force density, and another method is used to treat the singular transmission force density. For instance, because the transmission force density of the partitioned formulation is defined on a closed surface, it may be possible to treat it with higher-order accuracy by a version of the immersed interface method [53–58]. Such an extension of this method could yield a fully second-order accurate generalization of the IB method for problems, like those considered in this work, in which the immersed structure is of codimension zero with respect to the fluid.

Acknowledgements

This work was sponsored in part by an award from the Royal Society of Edinburgh. B.E.G. acknowledges research support from the American Heart Association (AHA award 10SDG4320049) and the National Science Foundation (NSF awards DMS-1016554 and OCI-1047734). He also gratefully ac-

knowledges discussions of this work with Charles Peskin and David McQueen. X.Y.L. acknowledges research support from the Engineering and Physical Sciences Research Council (EPSRC awards EP/G015651 and EP/I029990). Computations were performed at New York University using computer facilities funded in large part by a generous donation by St. Jude Medical, Inc.

References

- [1] C. S. Peskin, Flow patterns around heart valves: A digital computer method for solving the equations of motion, Ph.D. thesis, Albert Einstein College of Medicine (1972).
- [2] C. S. Peskin, Numerical analysis of blood flow in the heart, *J Comput Phys* 25 (3) (1977) 220–252.
- [3] C. S. Peskin, The immersed boundary method, *Acta Numer* 11 (2002) 479–517.
- [4] G. Iaccarino, R. Verzicco, Immersed boundary technique for turbulent flow simulations, *Appl Mech Rev* 56 (3) (2003) 331–347.
- [5] R. Mittal, G. Iaccarino, Immersed boundary methods, *Annu Rev Fluid Mech* 37 (2005) 239–261.
- [6] L. A. Miller, C. S. Peskin, When vortices stick: an aerodynamic transition in tiny insect flight, *J Exp Biol* 207 (17) (2004) 3073–3088.
- [7] L. A. Miller, C. S. Peskin, A computational fluid dynamics of ‘clap and fling’ in the smallest insects, *J Exp Biol* 208 (2) (2005) 195–212.
- [8] A. L. Fogelson, R. D. Guy, Immersed-boundary-type models of intravascular platelet aggregation, *Comput Meth Appl Mech Eng* 197 (25–28) (2008) 2087–2104.
- [9] X. Yang, R. H. Dillon, L. J. Fauci, An integrative computational model of multiciliary beating, *Bull Math Biol* 70 (4) (2008) 1192–1215.
- [10] C.-Y. Hsu, R. Dillon, A 3D motile rod-shaped monotrichous bacterial model, *Bull Math Biol* 71 (5) (2009) 1228–1263.
- [11] L. A. Miller, C. S. Peskin, Flexible clap and fling in tiny insect flight, *J Exp Biol* 212 (19) (2009) 3076–3090.
- [12] C. S. Peskin, D. M. McQueen, Fluid dynamics of the heart and its valves, in: H. G. Othmer, F. R. Adler, M. A. Lewis, J. C. Dallon (Eds.), *Case Studies in Mathematical Modeling: Ecology, Physiology, and Cell Biology*, Prentice-Hall, Englewood Cliffs, NJ, USA, 1996, pp. 309–337.

- [13] D. M. McQueen, C. S. Peskin, Shared-memory parallel vector implementation of the immersed boundary method for the computation of blood flow in the beating mammalian heart, *J Supercomput* 11 (3) (1997) 213–236.
- [14] J. D. Lemmon, A. P. Yoganathan, Three-dimensional computational model of left heart diastolic function with fluid-structure interaction, *J Biomech Eng* 122 (2) (2000) 109–117.
- [15] J. D. Lemmon, A. P. Yoganathan, Computational modeling of left heart diastolic function: Examination of ventricular dysfunction, *J Biomech Eng* 122 (4) (2000) 297–303.
- [16] D. M. McQueen, C. S. Peskin, A three-dimensional computer model of the human heart for studying cardiac fluid dynamics, *Comput Graph* 34 (1) (2000) 56–60.
- [17] D. M. McQueen, C. S. Peskin, Heart simulation by an immersed boundary method with formal second-order accuracy and reduced numerical viscosity, in: H. Aref, J. W. Phillips (Eds.), *Mechanics for a New Millennium, Proceedings of the 20th International Conference on Theoretical and Applied Mechanics (ICTAM 2000)*, Kluwer Academic Publishers, 2001.
- [18] B. E. Griffith, R. D. Hornung, D. M. McQueen, C. S. Peskin, An adaptive, formally second order accurate version of the immersed boundary method, *J Comput Phys* 223 (1) (2007) 10–49.
- [19] B. E. Griffith, X. Luo, D. M. McQueen, C. S. Peskin, Simulating the fluid dynamics of natural and prosthetic heart valves using the immersed boundary method, *Int J Appl Mech* 1 (1) (2009) 137–177.
- [20] X. Y. Luo, B. E. Griffith, X. S. Ma, M. Yin, T. J. Wang, C. L. Liang, P. N. Watton, G. M. Bernacca, Effect of bending rigidity in a dynamic model of a polyurethane prosthetic mitral valve, *Biomech Model Mechanobiology* (in press).
- [21] C. S. Peskin, The Immersed Boundary Method. III. Energy Functions for the Representation of Immersed Elastic Boundaries and Materials, handwritten lecture notes available from http://math.nyu.edu/faculty/peskin/ib_lecture_notes/index.html (2007).
- [22] D. Devendran, C. S. Peksin, An energy-based immersed boundary method for incompressible viscoelasticity (submitted).
- [23] L. Zhang, A. Gerstenberger, X. Wang, W. K. Liu, Immersed finite element method, *Comput Meth Appl Mech Eng* 193 (21–22) (2004) 2051–2067.
- [24] W. K. Liu, Y. Liu, D. Farrell, L. Zhang, X. S. Wang, Y. Fukui, N. Patankar, Y. Zhang, C. Bajaj, J. Lee, J. Hong, X. Chen, H. Hsu, Immersed finite element method and its applications to biological systems, *Comput Meth Appl Mech Eng* 195 (13–16) (2006) 1722–1749.

- [25] L. T. Zhang, M. Gay, Immersed finite element method for fluid-structure interactions, *J Fluid Struct* 23 (6) (2007) 839–857.
- [26] D. Boffi, L. Gastaldi, L. Heltai, C. S. Peskin, On the hyper-elastic formulation of the immersed boundary method, *Comput Meth Appl Mech Engrg* 197 (25–28) (2008) 2210–2231.
- [27] T. Belytschko, W. K. Liu, B. Moran, *Nonlinear Finite Elements for Continua and Structures*, John Wiley & Sons, Hoboken, NJ, USA, 2000.
- [28] B. E. Griffith, C. S. Peskin, On the order of accuracy of the immersed boundary method: Higher order convergence rates for sufficiently smooth problems, *J Comput Phys* 208 (1) (2005) 75–105.
- [29] IBAMR: An adaptive and distributed-memory parallel implementation of the immersed boundary method, <http://ibamr.googlecode.com>.
- [30] B. E. Griffith, On the volume conservation of the immersed boundary method, *Commun Comput Phys* (to appear, preprint available from <http://www.cims.nyu.edu/griffith>).
- [31] B. E. Griffith, An accurate and efficient method for the incompressible Navier-Stokes equations using the projection method as a preconditioner, *J Comput Phys* 228 (20) (2009) 7565–7595.
- [32] W. J. Rider, J. A. Greenough, J. R. Kamm, Accurate monotonicity- and extrema-preserving methods through adaptive nonlinear hybridizations, *J Comput Phys* 225 (2) (2007) 1827–1848.
- [33] P. Colella, P. R. Woodward, The piecewise parabolic method (PPM) for gas-dynamical simulations, *J Comput Phys* 54 (1) (1984) 174–201.
- [34] Y. Saad, A flexible inner-outer preconditioned GMRES algorithm, *SIAM J Sci Comput* 14 (2) (1993) 461–469.
- [35] SAMRAI: Structured Adaptive Mesh Refinement Application Infrastructure, <http://www.llnl.gov/CASC/SAMRAI>.
- [36] R. D. Hornung, S. R. Kohn, Managing application complexity in the SAMRAI object-oriented framework, *Concurrency Comput Pract Ex* 14 (5) (2002) 347–368.
- [37] R. D. Hornung, A. M. Wissink, S. R. Kohn, Managing complex data and geometry in parallel structured AMR applications, *Eng Comput* 22 (3–4) (2006) 181–195.
- [38] S. Balay, K. Buschelman, W. D. Gropp, D. Kaushik, M. G. Knepley, L. C. McInnes, B. F. Smith, H. Zhang, PETSc Web page, <http://www.mcs.anl.gov/petsc> (2009).
- [39] S. Balay, K. Buschelman, V. Eijkhout, W. D. Gropp, D. Kaushik, M. G. Knepley, L. C. McInnes, B. F. Smith, H. Zhang, PETSc users manual, Tech. Rep. ANL-95/11 - Revision 3.0.0, Argonne National Laboratory (2008).

- [40] S. Balay, V. Eijkhout, W. D. Gropp, L. C. McInnes, B. F. Smith, Efficient management of parallelism in object oriented numerical software libraries, in: E. Arge, A. M. Bruaset, H. P. Langtangen (Eds.), *Modern Software Tools in Scientific Computing*, Birkhäuser Press, 1997, pp. 163–202.
- [41] *hypre*: High performance preconditioners, <http://www.llnl.gov/CASC/hypre>.
- [42] R. D. Falgout, U. M. Yang, *hypre*: a library of high performance preconditioners, in: P. M. A. Sloot, C. J. K. Tan, J. J. Dongarra, A. G. Hoekstra (Eds.), *Computational Science - ICCS 2002 Part III*, Vol. 2331 of *Lecture Notes in Computer Science*, Springer-Verlag, 2002, pp. 632–641, also available as LLNL Technical Report UCRL-JC-146175.
- [43] *libMesh*: C++ Finite Element Library, <http://libmesh.sourceforge.net>.
- [44] B. Kirk, J. W. Peterson, R. H. Stogner, G. F. Carey, *libMesh*: A C++ library for parallel adaptive mesh refinement/coarsening simulations, *Eng Comput* 22 (3–4) (2006) 237–254.
- [45] O. Botella, R. Peyret, Benchmark spectral results on the lid-driven cavity flow, *Comput Fluid* 27 (4) (1998) 421–433.
- [46] H. Zhao, J. B. Freund, R. D. Moser, A fixed-mesh method for incompressible flow-structure systems with finite solid deformations, *J Comput Phys* 227 (6) (2008) 3114–3140.
- [47] X. Wang, L. T. Zhang, Interpolation functions in the immersed boundary and finite element methods, *Comput Mech* 45 (4) (2010) 321–334.
- [48] H. F. Liu, X. Y. Luo, Z. X. Cai, Stability and energy budget of pressure-driven collapsible channel flows, *J Fluid Mech* (in press).
- [49] Z. X. Cai, X. Y. Luo, A fluid beam model for flow in collapsible channels, *J Fluid Struct* 17 (1) (2003) 123–144.
- [50] S. Turek, J. Hron, Proposal for numerical benchmarking of fluid-structure interaction between an elastic object and laminar incompressible flow, in: H. J. Bungartz, M. Schäfer (Eds.), *Fluid-Structure Interaction: Modelling, Simulation, Optimization*, no. 53 in *Lecture Notes in Computational Science and Engineering*, Springer, 2006, pp. 371–385.
- [51] S. Turek, J. Hron, M. Razzaq, H. Wobker, M. Schäfer, Numerical benchmarking of fluid-structure interaction: A comparison of different discretization and solution approaches, Tech. rep., Fakultät für Mathematik, TU Dortmund, ergebnisberichte des Instituts für Angewandte Mathematik, Nummer 405 (2010).
- [52] E. P. Newren, A. L. Fogelson, R. D. Guy, R. M. Kirby, Unconditionally stable discretizations of the immersed boundary equations, *J Comput Phys* 222 (2) (2007) 702–719.

- [53] R. J. LeVeque, Z. Li, Immersed interface methods for Stokes flow with elastic boundaries or surface tension, *SIAM J Sci Comput* 18 (3) (1997) 709–735.
- [54] Z.-L. Li, M.-C. Lai, The immersed interface method for the Navier-Stokes equations with singular forces, *J Comput Phys* 171 (2) (2001) 822–842.
- [55] L. Lee, R. J. LeVeque, An immersed interface method for incompressible Navier-Stokes equations, *SIAM J Sci Comput* 25 (3) (2003) 832–856.
- [56] S. Xu, Z. J. Wang, An immersed interface method for simulating the interaction of a fluid with moving boundaries, *J Comput Phys* 216 (2) (2006) 454–493.
- [57] S. Xu, Z. J. Wang, Systematic derivation of jump conditions for the immersed interface method in three-dimensional flow simulation, *SIAM J Sci Comput* 27 (6) (2006) 1948–1980.
- [58] S. Xu, Z. J. Wang, A 3D immersed interface method for fluid-solid interaction, *Comput Meth Appl Mech Eng* 197 (2008) 2068–2086.